An Extended Calibration of the Olivine–Spinel Aluminum Exchange Thermometer: Application to the Melting Conditions and Mantle Lithologies of Large Igneous Provinces

Yishen Zhang [1,*], Olivier Namur[1], Weiran Li[2,3], Oliver Shorttle[2], Esteban Gazel[4], Eleanor Jennings[5], Peter Thy[6],

Timothy L. Grove[7] and Bernard Charlier[8]

[1]Department of Earth and Environmental Sciences, KU Leuven, 3000 Leuven, Belgium
[2]Department of Earth Sciences, University of Cambridge, Downing Street, Cambridge CB2 3EQ, UK
[3]Department of Earth Sciences, University of Hong Kong, Pokfulam Road, Hong Kong, 999077, China
[4]Department of Earth and Atmospheric Sciences, Cornell University, Ithaca, NY, 14853, USA
[5]Department of Earth and Planetary Sciences, Birkbeck, University of London, Malet Street, London WC1E 7HX, UK
[6]Department of Earth and Planetary Sciences, University of California, Davis, CA 95616, USA
[7]Department of Earth, Atmospheric and Planetary Sciences, Massachusetts Institute of Technology, 77 Massachusetts Avenue, Cambridge, 02139 Massachusetts, USA
[8]Department of Geology, University of Liège, 4000 Sart Tilman, Belgium

*Corresponding author. E-mail: yishen.zhang@kuleuven.be

Abstract

The application of the olivine–spinel aluminum exchange thermometer to natural samples is limited by the restricted experimental data set on which it was calibrated. Here, we present a new data set of 46 high-temperature crystallization experiments and 21 reanalyzed published experiments, which we used to extend the calibration to higher and lower temperatures. The final calibration data set spans a range of conditions relevant to crustal and upper mantle processes: 1174–1606°C, 0.1–1350 MPa, QFM − 2.5 to QFM + 7.2 (oxygen fugacity, fO$_2$, reported in log units relative to the quartz–fayalite–magnetite buffer, QFM), and 0–7.4 wt % H$_2$O$_{melt}$. We propose three new models. The first is thermodynamically self-consistent, based on spinel Fe, Mg, Al, and Cr compositions and Al exchange between olivine and spinel. The second and third are empirical models that consider fewer elemental exchanges: the second uses only Al exchange and spinel compositions, whereas the third considers olivine–spinel Al and Cr exchange. All models include the modest effect of pressure on olivine-spinel equilibrium chemistry, whereas fO$_2$ and water content have negligible effects. In general, as fewer elements are considered in the olivine–spinel exchange, the fit to experimental data worsens. Conversely, the associated decrease in model complexity improves their robustness against systematic errors when applied to natural crystal pairs: the thermodynamic model may underestimate crystallization temperatures in natural samples due to spinel subsolidus re-equilibration, whereas the empirical models (independent of Fe and Mg in spinel) are less sensitive to re-equilibration but yield temperatures with larger uncertainties. We applied a statistical test to select the most appropriate model for application to natural samples. When applied to lavas from mid-ocean ridges, Iceland, Skye, Emeishan, Etendeka, and Tortugal, our new temperature estimates are 30–100°C lower than previously proposed. The lower temperature estimates cause a lower mantle melting temperature and significant impacts on the mantle lithology constraints.

Key words: Cr-spinel; large igneous province; mantle melting; olivine; thermometry

INTRODUCTION

In the mantle, convection and upwelling plumes generate substantial magma volumes in mid-ocean ridge (MOR) systems and can produce oceanic or continental large igneous provinces (LIPs; e.g. Morgan, 1971; White & McKenzie, 1989; Campbell & Griffiths, 1990). Buoyantly ascending plume materials melt at relatively shallow depths (Sleep, 1992, 1996), eventually producing large volumes of magma through decompression melting of the plume head. Mantle plumes are sustained by temperature-induced density differences (e.g. Rayleigh–Taylor instability) compared to the ambient mantle (White & McKenzie, 1995), and large thermal anomalies (ca. 100–200°C; White & McKenzie, 1989) are generally

considered requisite for LIP activity. This thermal anomaly is commonly expressed as the excess temperature (T_{ex}), which is the difference between the mantle potential temperature (T_p, the mantle temperature extrapolated along the adiabat at 1 bar without melting; McKenzie & Bickle, 1988) at hotspots and of the ambient mantle (i.e. average MORs, $T_p \approx 1330$°C; e.g. Green & Falloon, 2005; Falloon *et al.,* 2007), where melts are generated by near-adiabatic upwelling of the upper mantle (McKenzie & Bickle, 1988).

The temperatures of LIP mantle sources have often been estimated by applying olivine-liquid geothermometers (Beattie, 1993; Putirka, 2005, 2008) to picritic basalts containing forsteritic olivine

(forsterite content expressed as $Fo = 100 \times$ molar $Mg/[Mg + Fe]$) to calculate the olivine-melt equilibrium temperature and then T_p (Putirka *et al.*, 2007). Other approaches involve modeling mantle melting as a function of pressure and temperature and comparing the modeled primary magmas with those determined from natural (near-) primary melts (Ghiorso & Sack, 1995; Ghiorso *et al.*, 2002; Herzberg & Asimow, 2015; Brown Krein *et al.*, 2021). However, these models require assumptions of primary melt compositions, even though near-primary melts rarely erupt (O'Hara, 1968; Neave *et al.*, 2019; Neave & Namur, 2022). Therefore, primary melt compositions are usually estimated by adding or subtracting an olivine component iteratively based on olivine-melt Fe–Mg exchange until equilibrium with a mantle Fo target is attained, often leading to large uncertainties in the FeO and MgO contents of the calculated primary melt (e.g. Herzberg *et al.*, 2007).

The olivine-spinel aluminum exchange thermometer (hereafter OSAT; Wan *et al.*, 2008; Coogan *et al.*, 2014) is based on the exchange of Al between olivine and spinel, written as $K_{DAl} = [Al_2O_3]_{Ol}/[Al_2O_3]_{Spl}$ (Al_2O_3 concentrations in wt %). This thermometer obviates the need to assume a melt composition because it determines the crystallization temperature directly from the equilibrium compositions of olivine and coexisting spinel. However, the OSAT was only calibrated at low pressure (0.1 MPa) and a restricted range of dry melt compositions (SiO_2, 40.5–45.9 wt %; MgO, 17.5–23.5 wt %; FeO, 10.6–12.2 wt %; Al_2O_3, 9.0–15.4 wt %), olivine compositions (Fo_{86-100}), spinel compositions (Cr# = 0–0.69, where Cr# = molar $Cr/[Cr + Al]$), and oxygen fugacities ($fO_2 = QFM - 1.5$ to $QFM + 0.5$, with 70% of the experiments performed at $QFM - 1.5$; QFM indicates the quartz–fayalite–magnetite equilibrium). Therefore, its applicability in diverse geological settings, particularly those with Cr-rich spinel in equilibrium with Fo-rich olivine, is questionable; it is unknown how intensive parameters such as pressure, fO_2, and volatile contents affect the OSAT calibration.

In this study, we performed and analyzed new experiments, reanalyzed prior experiments, and combined our results with the high-quality measurements of Wan *et al.* (2008) and Coogan *et al.* (2014) to extend the OSAT calibration. Our final experimental database spans 0.1 to 1350 MPa, 1174–1606°C, and $QFM - 2.5$ to $QFM + 7.2$ (i.e. air), and includes three hydrous experiments containing 3.7–7.4 wt % H_2O_{melt}.

We also developed a thermodynamic formalism to better understand olivine–spinel Al exchange. Our model suggests that, besides K_{DAl} and spinel Cr#, other components involving Fe and Mg in spinel have a significant impact on the calculated olivine–spinel equilibrium temperature and therefore on the previous OSAT calibration. This model is expected to be the most accurate parameterization for olivine and spinel compositions that quenched rapidly, inhibiting Mg–Fe exchange during cooling. However, this comprehensive thermodynamic model may retrieve systematically low temperature estimates when applied to natural rocks due to subsolidus olivine–spinel Fe–Mg re-equilibration. Therefore, we also report two empirical expressions that may be less prone to underestimating olivine–spinel equilibration temperatures in variably re-equilibrated natural samples, but are less precise and accurate than the thermodynamic model. The first empirical model follows a similar formalism as Coogan *et al.* (2014), only involving K_{DAl} and spinel Cr#. The second incorporates the exchange of Cr between olivine and spinel ($K_{DCr} = [Cr_2O_3]_{Ol}/[Cr_2O_3]_{Spl}$, Cr_2O_3 concentrations in wt %), which improves the accuracy of this model. We find that pressure has a moderate impact on the temperature calculations in all models, whereas fO_2 and water have negligible effects.

We applied our new models to re-constrain the crystallization temperature for published olivine-spinel pairs in natural rocks. A multi-component mantle melting model (Phipps Morgan, 2001; Shorttle *et al.*, 2014) is then applied to match crystallization temperature with geochemical constraints to estimate mantle temperatures and mantle lithology components (Matthews *et al.*, 2016, 2021). Our results suggest that previous studies using the model of Coogan *et al.* (2014) may have overestimated the crystallization temperature of olivine by as much as ~30–100°C for intra-plate LIPs, significantly overestimating T_p and impacting constraints on the mantle lithology. Based on our results, we provide new constraints on mantle melting conditions and mantle lithologies for MORs, Iceland, Skye, and intra-plate LIPs including Emeishan, Etendeka, and Tortugal.

The olivine-spinel aluminum exchange thermometer (OSAT)

The OSAT (Wan *et al.*, 2008; Coogan *et al.*, 2014) determines the equilibrium temperature of olivine-spinel pairs, which corresponds to the minimum saturation temperature of these two phases near the liquidus of their primitive parental melts (e.g. Jennings *et al.*, 2019). The crystallization temperature is calculated based on the concentration (in wt %) of Al_2O_3 in olivine and those of Al_2O_3 and Cr_2O_3 in spinel as:

$$T (K) = \frac{10,000}{0.575(0.162) + 0.884(0.043) \, Cr\# - 0.897(0.025) \, \ln (K_{DAl})} \tag{1}$$

with the standard errors on the determined coefficients reported in parentheses. The slow diffusion rate of Al_2O_3 in olivine minimizes the effect of re-equilibration at low temperatures (Spandler & O'Neill, 2010). The OSAT has been widely used to investigate the temperature of formation of terrestrial and extraterrestrial magmas (Gavrilenko *et al.*, 2016; Sobolev *et al.*, 2016; Prissel *et al.*, 2017; Trela *et al.*, 2017; Goltz *et al.*, 2020; Jennings *et al.*, 2020; Matthews *et al.*, 2021; Ramsey *et al.*, 2021;), including those of LIPs. However, the model has faced criticism for the limited experimental database used for its calibration, which has limited its application. The main issues with the previous calibration are: (1) the range of experimental spinel compositions is quite narrow compared to those observed in natural rocks (see next subsection); (2) the highest experimental temperature in the database (1450°C) is significantly lower than magmatic temperatures calculated in many natural settings (>1500°C; e.g. komatiite, Trela *et al.*, 2017; LIPs, Matthews *et al.*, 2021; Martian shergottites, Ramsey *et al.*, 2021), implying that the currently available expression must be extrapolated beyond its calibration range; and (3) high-pressure and hydrous experiments are absent in the calibration database.

Comparison of the original calibration experiments with natural rocks

To demonstrate the limitations of the existing olivine–spinel aluminum exchange calibration, we compare the olivine and spinel compositions used in the calibration experiments to those most common in LIPs.

To compare spinel compositions, we used the ternary projection of the spinel prism, $Al–Cr–Fe^{3+}$ (Fig. 1a). Spinel Fe^{3+} contents were calculated by charge balance on a four-oxygen basis (Droop, 1987). Both experimental and natural spinel compositions show a dominant trend from the Cr apex towards the Al apex. However, spinel in primitive basalts commonly have compositions plotting far beyond the calibration range (Cr# = 0.23–0.85 in natural spinel
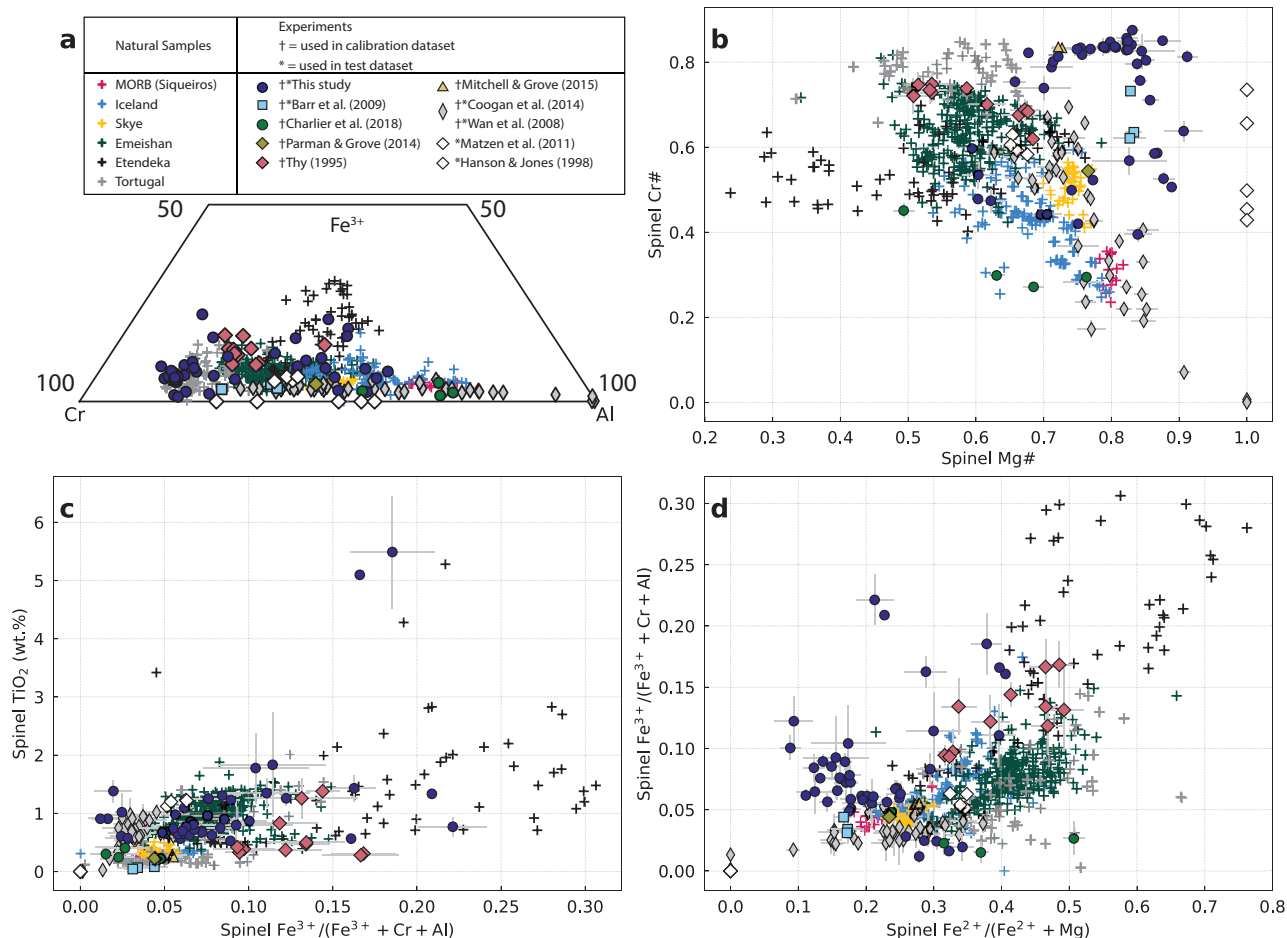
Fig. 1. Spinel compositions in calibration experiments and natural rocks. **(a)** Ternary projection of spinel prism, Al-Cr-Fe^{3+}. **(b)** Spinel Cr# as a function spinel Mg# **(c)** Spinel TiO_2 (wt %) as a function of spinel $Fe^{3+}/(Fe^{3+} + Cr + Al)$. **(d)** Spinel $Fe^{3+}/(Fe^{3+} + Cr + Al)$ as a function of spinel $Fe^{2+}/(Fe^{2+}+Mg)$. Data from Barr *et al.* (2009), Mitchell & Grove (2015), Charlier *et al.* (2018), Parman & Grove (2004), and Thy (1995) are remeasured published experiments. Data from Matzen *et al.* (2011) and Hanson & Jones (1998) are used as part of the test data set. See text for details on the calibration and test data set. Natural samples are compiled from published studies: MORB (Coogan *et al.,* 2014; Matthews *et al.,* 2021;), Iceland (Matthews *et al.,* 2016; Spice *et al.,* 2016), Skye (Spice *et al.,* 2016), Emeishan (Xu & Liu, 2016; Li *et al.,* 2021; Zhang *et al.,* 2021; Wu *et al.,* 2022), Etendeka (Jennings *et al.,* 2019), Tortugal (Trela *et al.,* 2017). † represents experiments used in the training data set, ∗ represents experiments used in the test data set. Error bar represents 1σ standard deviation and is not observable if it is smaller than the symbol.

vs. 0–0.69 in the calibration experiments; Fig. 1b). Natural spinel also has higher Fe^{3+} contents and occasionally higher TiO_2 contents (>5 wt %; Fig. 1c) compared to the calibration data set. Therefore, the experimental spinel compositions are only directly comparable to MORB compositions and partially overlap those from Iceland. The chemical composition of igneous spinel is known to be a complex function of intensive parameters (pressure, temperature, fO_2) and melt composition (Katsura & Ito, 1989; Ballhaus *et al.,* 1991; Ariskin & Nikolaev, 1996; Kamenetsky *et al.,* 2001). The chemical differences between experimental spinel compositions in the calibration data set and natural spinel may be due to the narrow fO_2 range and/or restricted melt compositions used in the experiments; many of the experiments were performed in the Cr-free simplified CaO–MgO–Al_2O_3–SiO_2 (CMAS) system, with pure spinel in equilibrium with forsterite. However, the observed differences could also be partly related to subsolidus Fe–Mg re-equilibration between olivine and spinel in natural rocks.

Figure 2 compares olivine Al_2O_3 and Cr_2O_3 concentrations as a function of Fo content. The restricted experimental conditions also limited the range of experimental olivine compositions to $Fo_{86–100}$ (Fo_{100} crystalized in CMAS experiments), compared to

the much wider range observed in natural olivine ($Fo_{68–94}$, Fig. 2). The Al_2O_3 (190–1519 μg/g) and Cr_2O_3 (165–3420 μg/g) contents of natural olivine crystals also commonly fall outside the calibration interval (Al_2O_3, 450–1686 μg/g; Cr_2O_3, 45–2990 μg/g).

EXPERIMENTAL STRATEGY AND ANALYTICAL METHODS
Selection and preparation of starting materials

To co-saturate olivine and spinel at different temperatures from a wide range of melt compositions, we used a variety of natural and synthetic starting compositions with 10.1–34.9 wt % MgO, 38.0–50.2 wt % SiO_2, 3.8–16.3 wt % Al_2O_3, 0.2–6.0 wt % total alkalis ($Na_2O + K_2O$) and 0.1–2.0 wt % Cr_2O_3. Details of the different starting compositions are reported in Table 1 and summarized here.

1) We used two komatiitic compositions from the Tortugal lava suite, Costa Rica: TO-080514-1 and TO-080514-2 (Trela *et al.,* 2017), here abbreviated as TO1 and TO2, respectively. These lavas have >33 wt % MgO, different TiO_2 contents (TO1:
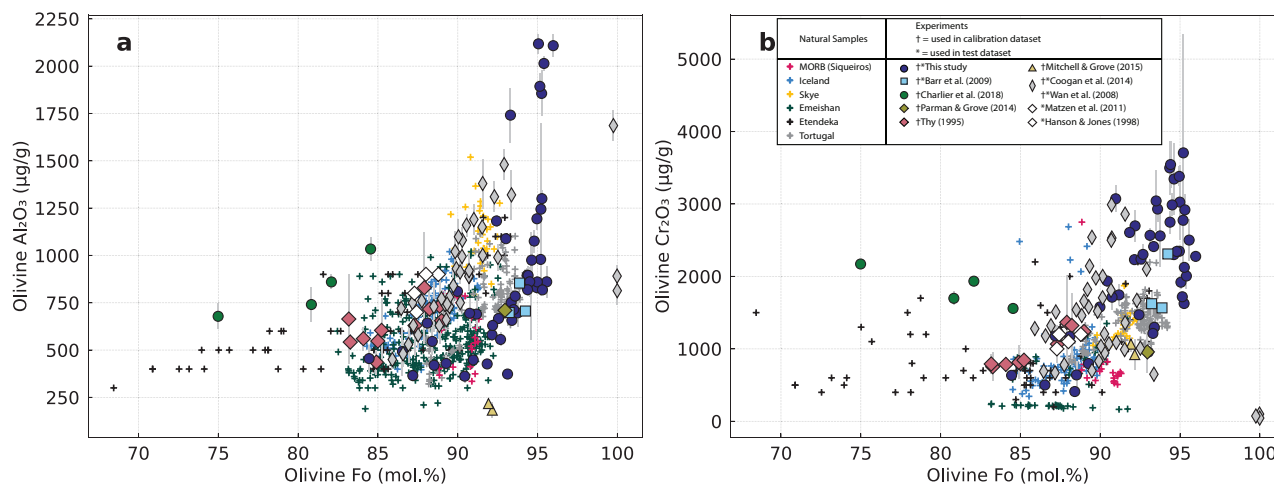
Fig. 2. (a) Al_2O_3 and **(b)** Cr_2O_3 concentrations in olivine (μg/g) as a function of Fo content (mol.%). Data sources are as in Fig. 1. Error bar represents 1σ standard deviation and is not observable if it is smaller than the symbol.

0.79 wt %; TO2: 0.89 wt %) and preserve olivine with high-Cr# spinel inclusions (Cr# >0.85).

2) Five basaltic compositions cover a range of melt SiO_2 (38.0–50.2 wt %,) and Al_2O_3 contents (3.8–16.3 wt %), which may affect the exchange of Al between the liquid, olivine, and spinel (Hanson & Jones, 1998; Evans *et al.*, 2008). These five compositions include: primitive basalts from Pico, Azores (PI052, van Gerve *et al.*, 2021) and Osorno volcano, Chile (OS082; Bechon *et al.*, 2022); two alkali-rich (>5 wt %), SiO_2-undersaturated basalts from Nyiragongo volcano, DR Congo (Ny17–135 and Ny17–161, Molendijk *et al.*, 2023a); and a porphyritic basalt from the Nyamuragira volcano, DR Congo (NYA2012–09-018, here abbreviated as NYAM).

3) We prepared three synthetic compositions as analogues to TO1, TO2, and Ny17–135 (Table 1). The objective here was to test the potential effect of relict olivine and spinel grains in natural materials with liquidus temperatures too high to completely melt in a standard muffle furnace prior to experimental runs in the vertical gas mixing furnace (see Experimental methods, below).

4) Finally, we synthesized the starting composition of Wan *et al.* (2008; here named 2Cr'+1Cr) to check interlaboratory experimental reproducibility and test analytical uncertainties under different analytical settings.

Natural samples were crushed to finer than 1 μm in a ball mill and melted three times at >1500°C in a Pt crucible in a muffle furnace: the first melting batch was used to saturate the Pt crucible and was not kept; the two additional batches were used to ensure the compositional homogeneity of the glass. The synthetic compositions were prepared from mixtures of high-purity oxides and silicates (SiO_2, TiO_2, Al_2O_3, MnO, MgO, Fe_2O_3, $CaSiO_3$, $AlPO_4$, Na_2SiO_3, $K_2Si_4O_9$, Cr_2O_3, NiO) in appropriate proportions. The silicates ($CaSiO_3$, Na_2SiO_3, and $K_2Si_4O_9$) were prepared following Zhang *et al.* (2023).

Due to the dramatic increase of Cr_2O_3 solubility in the melt (>1 wt %) at high temperatures (>1450°C; Borisova *et al.*, 2020) and the potential increase of the Cr_2O_3 evaporation rate with increasing temperature (Sossi *et al.*, 2019) in the gas mixing furnace, most natural and all synthetic compositions were doped with 1 to 2 wt % Cr_2O_3 (compositions with 'Cr1' suffixes for 1 wt % and 'Cr2' for 2 wt % dopant, respectively; Table 1). In some experiments, chromite and forsterite powders were added to change the liquidi

of olivine and spinel (Table 1). All starting powders were mixed and ground in ethanol for one hour then dried at 120°C before use in experiments.

Experimental methods

Experiments were conducted in a Nabertherm HTRV 50/150/17 vertical tube furnace at Katholieke Universiteit (KU) Leuven, Belgium, or a GERO HTRV 70–250/18 vertical tube furnace at the University of Liège, Belgium. Approximately 50 mg of starting material was suspended on a 0.2-mm diameter Pt loop. To avoid potential Fe loss, the Pt loops were pre-saturated with the experimental material for ~24 h at the same temperature and fO_2 to be used in the experiment, then cleaned with HF. Prior to experiments, all sample pellets were briefly heated in a muffle furnace at 1550°C to ensure sintering. Experimental samples were then suspended for 7–120 h in the hot spot of the vertical furnace (~5 cm in height, where temperature is stable to within ±3 and ±1°C in the Nabertherm HTRV 50/150/17 and GERO HTRV 70–250/18 furnaces, respectively). Temperature was measured using a S-type (Pt–$Pt_{90}Rh_{10}$) thermocouple calibrated against the melting points of Ag and Au. Oxygen fugacity was controlled using mixtures of high-purity CO and CO_2 flushed upward from the bottom of the alumina ceramic furnace tube. Bronkhorst gas-flow controllers were used to set the flow rate at 0.12 cm/s. The accuracy on the fO_2 was checked with a zirconia oxygen sensor. Because it is challenging to produce large spinel and olivine crystals above 1500°C, in experiments at such high temperatures, the temperature was first oscillated by ±10°C for ~1–2 h to increase the sizes of olivine and spinel crystals before holding the experiments isothermally for the remainder of the experiment. All experiments were drop-quenched in water. Experimental run conditions are detailed in Table 2.

Selection of previous experiments

To expand the experimental database and test the effects of pressure and water content on the Al exchange between olivine and spinel, we also selected and reanalyzed 21 published experiments, including crystallization experiments on Munro komatiite, Canada (Thy, 1995), lunar magma ocean (Charlier *et al.*, 2018), harzburgite melting experiments (Parman & Grove, 2004), hydrous melting experiments on komatiite from Commondale Ultramafic Suite, South Africa (Barr *et al.*, 2009), and melting experiments on

Table 1: Starting compositions used in this study

Sample Name	Index[a]	SiO$_2$	TiO$_2$	Al$_2$O$_3$	FeO$_t$	MnO	MgO	CaO	Na$_2$O	K$_2$O	P$_2$O$_5$	Cr$_2$O$_3$	Sum
natural rocks													
Ny17–135	A	40.53	1.33	6.91	12.21	0.18	28.14	8.18	1.03	0.70	0.44	0.35	100.00
Ny17–135_Cr2*	B	37.95	1.24	6.47	11.43	0.17	31.08	7.66	0.96	0.66	0.41	1.97	100.00
Ny17–161_Cr	C	39.67	3.19	10.61	11.50	0.22	10.99	16.30	3.01	2.97	1.48	0.06	100.00
Ny17–161_Cr2	D	39.11	3.14	10.46	11.34	0.21	10.84	16.07	2.97	2.93	1.46	1.48	100.00
NYAM_Cr2*	E	41.88	1.12	4.34	12.03	0.07	31.08	6.23	0.50	0.65	0.14	1.98	100.00
Os82	F	50.21	0.70	16.33	9.39	0.15	10.23	10.29	2.18	0.33	0.09	0.09	100.00
Os82_Cr	G	49.52	0.69	16.11	9.26	0.15	10.09	10.15	2.15	0.33	0.09	1.46	100.00
PI-052_Cr2*	H	39.42	0.86	4.35	7.39	0.12	32.93	12.68	0.10	0.11	0.06	1.98	100.00
TO1	I	44.77	0.79	3.94	11.88	0.17	32.86	4.82	0.12	0.05	0.19	0.42	100.00
TO1_Cr	J	44.62	0.79	3.93	11.84	0.17	32.74	4.80	0.12	0.05	0.19	0.78	100.00
TO1_Cr2	K	44.07	0.78	3.88	11.69	0.17	32.34	4.74	0.12	0.05	0.19	1.98	100.00
TO2	L	45.18	0.89	4.48	11.84	0.17	31.35	5.18	0.14	0.18	0.20	0.41	100.00
TO2_Cr	M	45.01	0.88	4.46	11.80	0.17	31.23	5.16	0.14	0.18	0.20	0.79	100.00
TO2_Cr2	N	44.46	0.87	4.41	11.66	0.17	30.85	5.10	0.14	0.18	0.20	1.98	100.00
synthetic material													
TO1_syn_Cr1	O	45.89	0.74	3.84	10.22	0.20	31.91	4.66	0.15	1.08	0.16	1.00	100.00
TO1_syn_Cr2	P	45.44	0.73	3.80	10.12	0.19	31.60	4.62	0.15	1.06	0.16	1.98	100.00
TO2_syn_Cr1	Q	43.73	2.26	4.86	11.60	0.24	34.87	0.56	0.22	0.20	0.21	1.00	100.00
TO2_syn_Cr2	R	43.30	2.23	4.81	11.49	0.24	34.52	0.56	0.22	0.20	0.21	1.98	100.00
Ny17_syn_Cr1	S	38.42	1.26	6.53	10.40	0.24	32.07	7.74	0.99	0.68	0.43	1.00	100.00
Ny17_syn_Cr2	T	38.04	1.25	6.47	10.30	0.24	31.75	7.66	0.98	0.67	0.43	1.98	100.00
2Cr' + 1Cr	U	45.01	0.84	9.69	12.31	0.10	22.71	7.67	1.00	0.04	0.11	0.52	100.00

[a]Indexes are used to indicate which starting composition was used during the experiments in Table. 2.
*Indicates starting composition was doped with forsterite or MgO to increase liquidus.

fertile mantle component (Mitchell & Grove, 2015). These experiments span a range of temperature between 1215 and 1350°C, pressure between 0.1 and 1350 MPa, fO_2 from QFM − 2.5 to QFM, and between 0 and 7.4 wt % H_2O_{melt}.

Analytical methods

Analyses were performed using a JEOL JXA-8530F Wavelength Dispersive Spectrometer (WDS) Field Emission Gun Electron probe micro-analyzer (EPMA) at the Department of Material Engineering, KU Leuven, Belgium, and a Cameca SX-100 Electron Microprobe at the Department of Earth Sciences, University of Cambridge. Major and trace elements were measured with different calibrations and analytical setups detailed in the Supplementary data and summarized here. Major element concentrations in olivine and spinel were generally within 98% accuracy of the reference values.

Experimental products were mounted in high-purity epoxy and polished for analysis. Electron probe micro-analyzer measurements of trace elements in olivine, especially Cr and Al, are known to suffer from secondary fluorescence from surrounding spinel or melt (Llovet et al., 2012; Gavrilenko et al., 2023; Llovet et al., 2023). We used FANAL (Llovet et al., 2012) and PENEPMA (Llovet & Salvat, 2017), Monte Carlo simulation tools to model coupled electron-photon transportation, and simulated analyses of San Carlos olivine and VG-2 glass standards. The results show that measuring olivine compositions at least 5 μm (based on FANAL) and 15 μm (based on PENEPMA) inward from the phase margin dramatically reduces the influence of secondary fluorescence (Fig. S1). This analytical strategy was applied to sufficiently large olivine (> 10 μm) crystals in the experimental charges. Analytical results for experiments with smaller olivine (∼ 10 μm) were manually filtered by removing anomalous outliers (see more details below).

At KU Leuven, Al, P, Cr, and Ca in olivine were measured with a focused beam operating at 20 kV and 300 nA and calibrated with a MongOl sh11–2 olivine (Batanova et al., 2019). Detection

limits were 6 μg/g for Al$_2$O$_3$, 9 μg/g for P$_2$O$_5$, and 4 μg/g for Cr$_2$O$_3$. High-precision wavelength scanning at 20 kV and 300 nA was performed prior to each session to accurately determine the Al, Cr, and P peak positions (Fig. S2). Background positions were chosen near (∼0.5 mm) the base of the peak to minimize the subtraction of background counts (Batanova et al., 2015). Because it is difficult to properly analyze major elements by WDS at high beam currents due to the high counting rates and the possibility of oversaturating the detectors, Si, Mg, and Fe in olivine and all elements in spinel were measured afterwards with a focused beam at 15 kV and 20 nA and calibrated with natural and synthetic primary standards (see Supplementary data). To ensure reproducibility between sessions, secondary standards (San Carlos olivine NMNH 111312–44 for olivine, chromite NMNH 117075 for spinel) were analyzed at regular intervals to correct for any instrumental drift. In the San Carlos olivine, we measured 338 ± 14 μg/g Al$_2$O$_3$ (1σ, $n = 72$), 43 ± 22 μg/g P$_2$O$_5$ (1σ), and 135 ± 9 μg/g Cr$_2$O$_3$ (1σ), which are comparable with the results of Batanova et al. (2015; 330 ± 10 μg/g Al$_2$O$_3$, 50 ± 10 μg/g P$_2$O$_5$, 152 ± 8 μg/g Cr$_2$O$_3$, uncertainties in 2σ). Glasses were analyzed at KU Leuven using a beam defocused to 10–30 μm diameter and operating at 15 kV and 10 nA. Quench textures were observed in the highest temperature experiments (>1500°C), which causes MgO depletion in the interstitial melt. For those experiments, melt compositions were measured on mixtures of melt and quenched crystals, increasing the 1σ standard deviations for melt MgO and FeO contents to 1.0 to 4.7 wt % and 0.4 to 1.3 wt %, respectively. Glass secondary standards NMNH 111312–44, VG2, and GOR 132-G (Jochum et al., 2006) were analyzed at regular intervals, and the results were again within 98% accuracy of the reference values (see supplementary data set). X-ray compositional maps were acquired following the procedure of Shea et al. (2019), but using a 20-kV and 300-nA electron beam.

At the University of Cambridge, we followed a similar procedure using a focused beam operating at 15 kV and 100 nA

Table 2: Experimental conditions of extended, re-measured and literature data

Run No.	Reference	T (°C)	Pressure (MPa)	logfO_2	ΔQFM	H2O (wt %)	Duration (h)
This study							
CAG03-K[a, b]	This study	1606.00	0.10	−4.53	0.00	0.00	7.00
CAG03-N[a]	This study	1606.00	0.10	−4.53	0.00	0.00	7.00
CAG03-H[a]	This study	1606.00	0.10	−4.53	0.00	0.00	7.00
CAG04-N[a]	This study	1568.00	0.10	−4.83	0.00	0.00	7.00
CAG04-E[a]	This study	1568.00	0.10	−4.83	0.00	0.00	7.00
CAG05-R[a]	This study	1571.00	0.10	−4.81	0.00	0.00	24.00
CAG05-S[a]	This study	1571.00	0.10	−4.81	0.00	0.00	24.00
CAG06-P[a]	This study	1571.00	0.10	−4.81	0.00	0.00	24.00
CAG06-R[a]	This study	1571.00	0.10	−4.81	0.00	0.00	24.00
CAG06-T[a]	This study	1571.00	0.10	−4.81	0.00	0.00	24.00
CAG07-T[a]	This study	1600.00	0.10	−4.58	0.00	0.00	24.00
NAB01-C	This study	1190.00	0.10	−8.53	0.00	0.00	72.00
NAB01-G	This study	1190.00	0.10	−8.53	0.00	0.00	72.00
NAB01-F	This study	1190.00	0.10	−8.53	0.00	0.00	72.00
NAB02-D	This study	1174.00	0.10	−8.72	0.00	0.00	94.00
NAB02-G	This study	1174.00	0.10	−8.72	0.00	0.00	94.00
NAB02-F	This study	1174.00	0.10	−8.72	0.00	0.00	94.00
NAB21-A	This study	1450.00	0.10	−5.84	0.00	0.00	24.00
NAB24-I	This study	1401.00	0.10	−6.29	0.00	0.00	72.00
NAB24-L	This study	1401.00	0.10	−6.29	0.00	0.00	72.00
NAB31-L	This study	1401.00	0.10	−4.29	2.00	0.00	48.00
NAB31-A	This study	1401.00	0.10	−4.29	2.00	0.00	48.00
NAB41-J	This study	1469.00	0.10	−5.67	0.00	0.00	48.00
NAB41-M	This study	1469.00	0.10	−5.67	0.00	0.00	48.00
NAB45-K[a, c]	This study	1529.00	0.10	−5.15	0.00	0.00	24.00
NAB45-N[a, c]	This study	1529.00	0.10	−5.15	0.00	0.00	24.00
NAB45-B[a, c]	This study	1529.00	0.10	−5.15	0.00	0.00	24.00
NAB45-H[a, c]	This study	1529.00	0.10	−5.15	0.00	0.00	24.00
NAB49-Q	This study	1500.00	0.10	−5.40	0.00	0.00	24.00
NAB49-R	This study	1500.00	0.10	−5.40	0.00	0.00	24.00
NAB51-R	This study	1500.00	0.10	−5.40	0.00	0.00	24.00
NAB51-S	This study	1500.00	0.10	−5.40	0.00	0.00	24.00
NAB52-R[a]	This study	1529.00	0.10	−5.15	0.00	0.00	24.00
NAB53-O	This study	1445.00	0.10	−5.89	0.00	0.00	72.00
NAB53-Q	This study	1445.00	0.10	−5.89	0.00	0.00	72.00
NAB53-R	This study	1445.00	0.10	−5.89	0.00	0.00	72.00
NAB53-S	This study	1445.00	0.10	−5.89	0.00	0.00	72.00
NAB57-R[a]	This study	1530.00	0.10	−5.15	0.00	0.00	24.00
NAB57-T[a]	This study	1530.00	0.10	−5.15	0.00	0.00	24.00
NAB58-R	This study	1397.00	0.10	−6.33	0.00	0.00	72.00
*NAB88-R	This study	1350.00	0.10	−8.39	−1.60	0.00	118.00
NAB89-U	This study	1253.00	0.10	−9.41	−1.60	0.00	120.00
*NAB89-R	This study	1253.00	0.10	−9.41	−1.60	0.00	120.00
NAB90-U	This study	1305.00	0.10	−8.85	−1.60	0.00	36.00
*NAB91-Q	This study	1305.00	0.10	−8.85	−1.60	0.00	36.00
*NAB91-R	This study	1305.00	0.10	−8.85	−1.60	0.00	36.00
Re-analyzed experiments			0.00				
com1–12	Barr *et al.* (2009)	1320.00	0.10	−7.09	0.00	0.00	
com1–2	Barr *et al.* (2009)	1350.00	0.10	−6.79	0.00	0.00	
com1–4	Barr *et al.* (2009)	1300.00	0.10	−7.30	0.00	0.00	
213.00	Thy (1995)	1240.00	0.10	−7.95	0.00	0.00	
214.00	Thy (1995)	1251.00	0.10	−7.83	0.00	0.00	
215.00	Thy (1995)	1231.00	0.10	−8.05	0.00	0.00	
216.00	Thy (1995)	1221.00	0.10	−8.17	0.00	0.00	
218.00	Thy (1995)	1200.00	0.10	−8.41	0.00	0.00	
224.00	Thy (1995)	1260.00	0.10	−7.73	0.00	0.00	
228.00	Thy (1995)	1279.00	0.10	−7.52	0.00	0.00	
230.00	Thy (1995)	1300.00	0.10	−7.30	0.00	0.00	
233.00	Thy (1995)	1311.00	0.10	−7.18	0.00	0.00	
234.00	Thy (1995)	1320.00	0.10	−7.09	0.00	0.00	
235.00	Thy (1995)	1328.00	0.10	−7.01	0.00	0.00	
c553	Mitchell & Grove (2015)	1215.00	1200.00	−8.78	−0.54	6.00	
c559	Mitchell & Grove (2015)	1250.00	1200.00	−8.42	−0.59	3.70	

(Continued)

Table 2: Experimental conditions of extended, re-measured and literature data

Run No.	Reference	T (°C)	Pressure (MPa)	log$f$O$_2$	ΔQFM	H2O (wt %)	Duration (h)
on66-ha04	Charlier et al. (2018)	1230.00	500.00	−10.58	−2.52	0.00	
twm-f0.6-b1255	Charlier et al. (2018)	1360.00	1350.00	−9.03	−2.34	0.00	
twm71-b1295	Charlier et al. (2018)	1300.00	800.00	−9.72	−2.42	0.00	
twm71-ha04	Charlier et al. (2018)	1230.00	500.00	−10.58	−2.52	0.00	
w7	Parman & Grove (2004)	1320.00	1200.00	−8.09	−1.00	7.40	
Literature data							
w39	Wan et al. (2008)	1250.00	0.10	−9.55	−1.71	0.00	
w83_1	Wan et al. (2008)	1250.00	0.10	−9.55	−1.71	0.00	
w83_2	Wan et al. (2008)	1250.00	0.10	−9.55	−1.71	0.00	
w83_3	Wan et al. (2008)	1250.00	0.10	−9.55	−1.71	0.00	
w83_4	Wan et al. (2008)	1250.00	0.10	−9.55	−1.71	0.00	
w83_5	Wan et al. (2008)	1250.00	0.10	−9.55	−1.71	0.00	
w83_6	Wan et al. (2008)	1250.00	0.10	−9.55	−1.71	0.00	
w83_7	Wan et al. (2008)	1250.00	0.10	−9.55	−1.71	0.00	
w35	Wan et al. (2008)	1300.00	0.10	−8.95	−1.65	0.00	
w71_1	Wan et al. (2008)	1300.00	0.10	−8.95	−1.65	0.00	
w71_2	Wan et al. (2008)	1300.00	0.10	−8.95	−1.65	0.00	
w72_1	Wan et al. (2008)	1300.00	0.10	−8.95	−1.65	0.00	
w72_2	Wan et al. (2008)	1300.00	0.10	−8.95	−1.65	0.00	
w73	Wan et al. (2008)	1300.00	0.10	−8.95	−1.65	0.00	
w36_1	Wan et al. (2008)	1350.00	0.10	−8.35	−1.56	0.00	
w36_2	Wan et al. (2008)	1350.00	0.10	−8.35	−1.56	0.00	
w55	Wan et al. (2008)	1350.00	0.10	−8.35	−1.56	0.00	
w55_1	Wan et al. (2008)	1350.00	0.10	−8.35	−1.56	0.00	
w55_2	Wan et al. (2008)	1350.00	0.10	−8.35	−1.56	0.00	
w62_1	Wan et al. (2008)	1350.00	0.10	−8.35	−1.56	0.00	
w62_2	Wan et al. (2008)	1350.00	0.10	−8.35	−1.56	0.00	
w66	Wan et al. (2008)	1350.00	0.10	−8.35	−1.56	0.00	
w66_1	Wan et al. (2008)	1350.00	0.10	−8.35	−1.56	0.00	
w61	Wan et al. (2008)	1400.00	0.10	−7.85	−1.55	0.00	
w61_1	Wan et al. (2008)	1400.00	0.10	−7.85	−1.55	0.00	
w86	Wan et al. (2008)	1400.00	0.10	−7.85	−1.55	0.00	
w86_1	Wan et al. (2008)	1400.00	0.10	−7.85	−1.55	0.00	
w86_2	Wan et al. (2008)	1400.00	0.10	−7.85	−1.55	0.00	
w60_1	Wan et al. (2008)	1450.00	0.10	−7.35	−1.51	0.00	
w60_2	Wan et al. (2008)	1450.00	0.10	−7.35	−1.51	0.00	
w78	Wan et al. (2008)	1450.00	0.10	−7.35	−1.51	0.00	
w328*	Coogan et al. (2014)	1250.00	0.10	−0.68	7.16	0.00	
w328*_1	Coogan et al. (2014)	1250.00	0.10	−0.68	7.16	0.00	
w290_1	Coogan et al. (2014)	1350.00	0.10	−0.68	6.11	0.00	
w330	Coogan et al. (2014)	1350.00	0.10	−0.68	0.49	0.00	
w330_1	Coogan et al. (2014)	1350.00	0.10	−6.30	0.49	0.00	
w330_2	Coogan et al. (2014)	1350.00	0.10	−6.30	0.49	0.00	
w332	Coogan et al. (2014)	1350.00	0.10	−7.30	−0.51	0.00	
w332_1	Coogan et al. (2014)	1350.00	0.10	−7.30	−0.51	0.00	
w338	Coogan et al. (2014)	1350.00	0.10	−5.50	1.29	0.00	
matzen2011_15	Matzen et al. (2011)	1349.00	0.10	−6.87	−0.07	0.00	
matzen2011_6	Matzen et al. (2011)	1302.00	0.10	−7.36	−0.08	0.00	
matzen2011_8	Matzen et al. (2011)	1302.00	0.10	−7.36	−0.08	0.00	
matzen2011_46	Matzen et al. (2011)	1300.00	0.10	−7.41	−0.11	0.00	
H&J_1998_FAD1b	Hanson & Jones (1998)	1320.00	0.10	−3.00	4.09	0.00	
H&J_1998_FAD2	Hanson & Jones (1998)	1320.00	0.10	−3.00	4.09	0.00	
H&J_1998_FAD3	Hanson & Jones (1998)	1320.00	0.10	−3.00	4.09	0.00	
H&J_1998_FAS1	Hanson & Jones (1998)	1320.00	0.10	−3.00	4.09	0.00	
H&J_1998_FAS1_1	Hanson & Jones (1998)	1320.00	0.10	−3.00	4.09	0.00	

[a]indicates 1–2 hour thermal oscillation (±10°C) was applied;
[b]Experiment number ends with the starting composition noted in Table. 1;
[c]indicates chromite seeds were applied.
*indicates experiments contain clinopyroxene

beam to measure Al, Cr, and P in olivine. Detection limits were 28 μg/g for Al$_2$O$_3$, 117 μg/g for P$_2$O$_5$, and 87 μg/g for Cr$_2$O$_3$. We used the MongOl sh11–2 olivine ($n=8$) as a secondary standard and obtained 487±10 μg/g Al$_2$O$_3$ (1σ), 228±40 μg/g P$_2$O$_5$ (1σ), and 209±20 μg/g Cr$_2$O$_3$ (1σ), again consistent with the reference values (463±18 μg/g Al$_2$O$_3$, 152±8 μg/g P$_2$O$_5$, 182±6 μg/g Cr$_2$O$_3$, uncertainties in 2σ; Batanova et al., 2019).
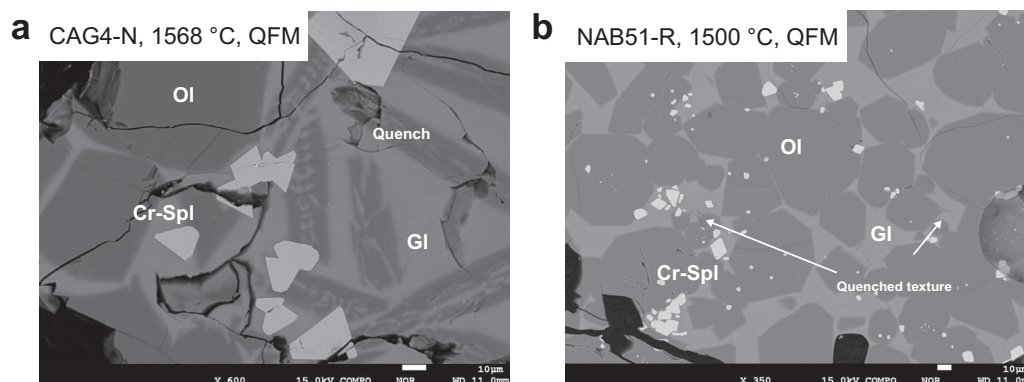
Fig. 3. Representative backscattered electron images of experimental products. Quench texture is observed in high temperature experiments (>1500°C), euhedral olivine and spinel indicate the attainment of equilibrium in the experiments. Abbreviations: Gl, glass; Cr-Spl, Cr-spinel; Ol, olivine.

Interlaboratory experimental and analytical uncertainties

To calibrate our extended OSAT with as many relevant experiments as possible, we chose to include the experimental results of Wan *et al.* (2008) and Coogan *et al.* (2014), which we could not reanalyze for this study. It is therefore important to critically assess whether we can reproduce their phase equilibria observations and reproduce their chemical measurements, including minor elements such as Al in olivine. Therefore, we reproduced two experiments from Wan *et al.* (2008): w83 (~QFM − 1.6, 1250°C), reproduced here in experiment NAB89U, and w71 (~QFM − 1.6, 1300°C), reproduced here in experiment NAB90U. We chose these two relatively low-temperature experiments because it is more challenging to attain equilibrium under those conditions.

Experiments NAB89U and NAB90U produced phase equilibria (liquid, olivine, and spinel) and compositions similar to those reported by Wan *et al.* (2008). Importantly, $\ln(K_{D_{Al}})$ values were almost identical: -6.16 ± 0.04 (1σ, uncertainty calculated from error propagation with a Monte Carlo algorithm) in NAB89U vs. -6.14 ± 0.05 (1σ) in w83, and -5.80 ± 0.03 (1σ) in NAB90U vs. -5.90 ± 0.05 (1σ) in w71. Spinel compositions were also identical: Fe^{3+}/Fe^{2+} in spinel was 0.16 ± 0.05 (1σ) in NAB89-U vs. 0.17 ± 0.09 (1σ) in w83, and 0.21 ± 0.03 (1σ) in NAB90-U vs. 0.21 ± 0.07 (1σ) in w71. This suggests that interlaboratory analytical and experimental uncertainties are minor, and further that we can include the published experimental results from Wan *et al.* (2008) and Coogan *et al.* (2014) in our new OSAT calibration database. This also suggests that our experiments attained equilibrium (see next subsection).

Attainment of equilibrium

The attainment of equilibrium between melt, olivine, and spinel, especially for slowly diffusing minor elements, is critical to our study. The considerably long durations of our experimental runs (7–120 h), most much longer than in high-temperature experiments in the previous calibration (Wan *et al.,* 2008) or other high-temperature experimental studies (e.g. Tuff *et al.,* 2005; Matzen *et al.,* 2011; Krasheninnikov *et al.,* 2017; Koshlyakova *et al.,* 2022), were chosen to ensure that equilibrium was attained. We note that a few high-temperature experiments (>1500°C, Table 2) lasted only a few hours (≥7 h), but that the fast elemental diffusion at such high temperatures and the low crystallinity of those experiments suggest that equilibrium was attained even in those shorter runs.

We also evaluated the attainment of equilibrium based on compositional and textural characteristics. Olivine and spinel were generally euhedral, suggesting they formed at equilibrium. The experimental charges also show homogeneous backscattered electron intensities for melts and minerals (Fig. 3). Fe–Mg partition coefficients between olivine and melt ($K_{D_{Fe-Mg}}^{Ol-melt}$) range from 0.26 to 0.34 (see in the Supplementary data), consistent with previous experiments (e.g. Roeder & Emslie, 1970; Toplis & Carroll, 1995) and thermodynamic models (e.g. Toplis, 2005; Blundy *et al.,* 2020). In general, $K_{D_{Fe-Mg}}^{Ol-melt}$ is positively correlated with the melt SiO_2 content, which supports the impact of melt silica activity on Fe–Mg exchange between olivine and melt (Gee & Sack, 1988; Toplis, 2005; Koshlyakova *et al.,* 2022). In particular, experiments using silica-undersaturated and alkali-rich compositions have $K_{D_{Fe-Mg}}^{Ol-melt} < 0.27$ (0.22–0.26), consistent with experimental results on similar compositions (Gee & Sack, 1988; Molendijk *et al.,* 2023b). In contrast, high-temperature experiments with quench textures occasionally have $K_{D_{Fe-Mg}}^{Ol-melt} = 0.34$–0.35, beyond the range 0.30 ± 0.03; such high values may have resulted from analytical heterogeneity due to the glass analyses involving mixtures of quench crystals and interstitial melt (Mitchell & Grove, 2015).

Trace element (Al, P, Cr) partitioning in olivine may be affected due to the formation of a boundary layer enrichment during initially rapid crystal growth (e.g. Shea *et al.,* 2019; Lang *et al.,* 2022). This means that the above indicators of equilibrium (Fe–Mg exchange and textural constraints) may not reflect trace element equilibrium. Therefore, we measured rim-to-core profiles comprising 6–7 spot analyses (ca. 5–6 μm spacing) per profile in one olivine crystal from each experiment to check the homogeneity of their trace element distributions. The profiles generally show very small deviations (~50 μg/g, 1σ) for Al_2O_3 and even less variability for other trace elements (see Supplementary material, Section 2). We also acquired EPMA X-ray compositional maps of experiments treated with thermal oscillation and experiments that were run at more than 200°C below their liquidi. Chemical maps do not show any apparent P, Al, or Cr zoning (see Supplementary material, Section 2). Relict phases were occasionally observed in the cores of olivine crystals in experiments performed on compositions with high liquidus temperatures. The uniform compositions of the crystal rims, however, suggest that the early disequilibrium did not preclude the attainment of equilibrium between the outer part of the crystals and the adjacent melt. Experiments conducted at more than 300°C below the liquidus typically produced small olivine crystals (~10 μm in length) with dendritic P and Al zoning patterns. These experiments also produce olivine populations
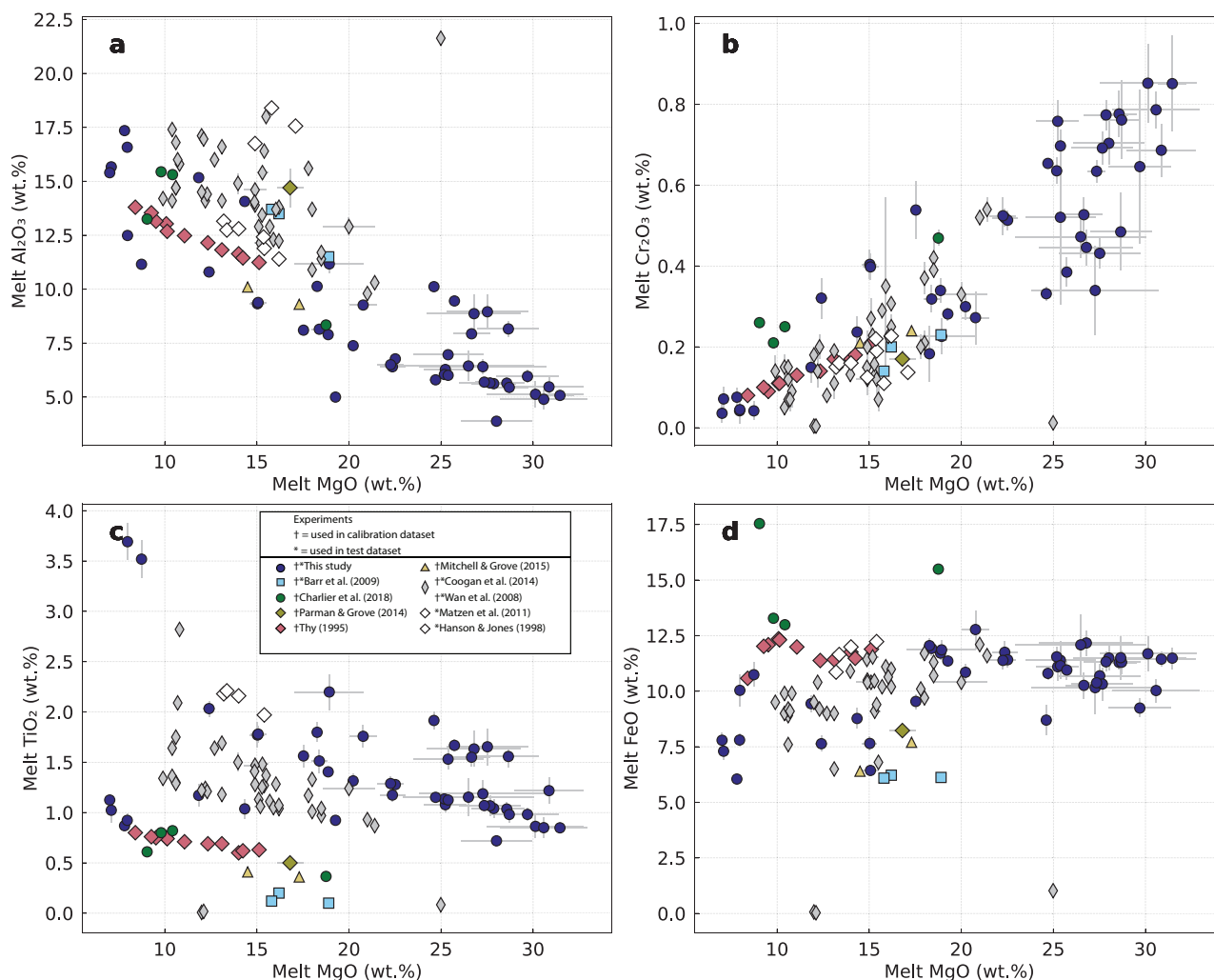
Fig. 4. Melt compositional variations as functions of melt MgO content (wt %). Experimental data sources are as in Fig. 1. Error bar represents 1σ standard deviation and is not observable if it is smaller than the symbol.

with distinct high and low Al_2O_3 concentrations; we used the low-concentration population in this study because it may represent relaxation and equilibration during equilibrium crystal growth (Shea *et al.,* 2019).

RESULTS
Experimental results

All reported experiments contain melt, olivine, and spinel. Four experiments performed at more than 300°C below the liquidus also contain clinopyroxene. Compositions of the phases are given in supplementary data set (Table S1).

Melt

Melt compositions are plotted as functions of MgO (in wt %) and temperature in Figs. 4 and S3, respectively. The experimental melts span a wide range of compositions, with 7.0–31.5 wt % MgO, 38.9–54.6 wt % SiO_2, 6.0–12.8 wt % FeO, 3.9–17.3 wt % Al_2O_3, 0.0–0.9 wt % Cr_2O_3, and 0.1–4.6 wt % $Na_2O + K_2O$. Melt Al_2O_3 contents are anticorrelated with melt MgO content, whereas melt Cr_2O_3 contents are positively correlated with melt MgO content and temperature, consistent with the higher solubility of Cr_2O_3 in the melt at higher temperature (Borisova *et al.,* 2020).

Olivine

Olivine crystals are euhedral and ranged in size from ~10 μm to >100 μm (Fig. 3). Olivine Fo contents range from Fo_{84} to Fo_{96} (Fig. 2). Minor and trace elements span a wide compositional range: 0.1–1.3 wt % CaO, 362–2118 μg/g Al_2O_3, 411–3706 μg/g Cr_2O_3, and below the detection limit to 511 μg/g P_2O_5. Al_2O_3 and Cr_2O_3 contents are weakly correlated with Fo content (Fig. 2). Olivine Cr_2O_3 content is positively correlated with melt Cr_2O_3 content (Fig. S4b). A broad positive correlation is also observed between olivine and melt CaO contents (Fig. S4c), and the highest olivine CaO contents occur in experiments on SiO_2-undersaturated compositions, consistent with previous findings (Gee & Sack, 1988; Molendijk *et al.,* 2023b). No correlation is apparent between olivine and melt Al_2O_3 or P_2O_5 contents (Fig. S4a, d, respectively).

Spinel

Spinel crystals range in size from ~1 μm to ~40 μm (Fig. 3). Spinel compositions are shown in Figs. 1 and in Fig. S5 as functions of melt composition. Spinel Cr# ranges from 0.40 to 0.88, Mg# [= molar $Mg/(Mg + Fe^{2+})$] from 0.59 to 0.91, Fe^{3+}/Fe^{2+} from 0.08 to 2.48, the ratio of Fe^{3+} to the sum of trivalent cations, $Fe^{3+}/(Fe^{3+} + Cr + Al)$, from 0.02 to 0.22, and TiO_2 content from

0.5 to 5.5 wt %. Experiments NAB01-F and NAB02-F, performed on SiO_2-undersaturated and alkali-rich compositions, show the highest spinel TiO_2 contents (>5 wt %), which correspond to the highest melt TiO_2 contents (>3 wt %; Fig. S5). Spinel FeO and Cr_2O_3 contents are only weakly correlated with melt FeO and Cr_2O_3 contents (Fig. S5). A more significant correlation is observed between spinel and melt Al_2O_3 contents (Fig. S5), consistent with previous observations (Sack & Ghiorso, 1991b; Ariskin & Nikolaev, 1996; Poustovetov & Roeder, 2001; Borisova et al., 2020).

Summary of remeasured prior experiments

Melt compositions in the reanalyzed published experiments and calibrations contain 8.4–25.0 wt % MgO, 42.0–55.6 wt % SiO_2, 0–17.5 wt % FeO, 8.3–21.6 wt % Al_2O_3, and 0–0.54 wt % Cr_2O_3. Olivine has $Fo_{75–100}$ and contain 0–1.4 wt % CaO, 183–1686 $\mu g/g$ Al_2O_3, 0–2990 $\mu g/g$ Cr_2O_3, and 0–2338 $\mu g/g$ P_2O_5. Spinel has Cr# = 0–0.84, Mg# = 0.49–1, Fe^{3+}/Fe^{2+} = 0.08–0.71, $Fe^{3+}/(Fe^{3+} + Cr + Al)$ = 0–0.17, and contains 0–1.38 wt % TiO_2.

Evaluating the model of Coogan et al. (2014)

We assessed the OSAT of Coogan et al. (2014), which incorporates the earlier experiments of Wan et al. (2008), by applying it to our updated experimental data set (Fig. 5a). The results show that the model of Coogan et al. (2014) significantly overestimated temperatures, with a maximum deviation (ΔT [°C] = predicted temperature − measured temperature) of 197°C, an average deviation of 44.7 ± 46.6°C (1σ), and a root-mean-square error (RMSE) of ±64.3°C. These errors further demonstrate the need for a new calibration covering a broader temperature range and accounting for additional factors affecting olivine–spinel Al exchange, including spinel composition, fO_2, pressure, and melt H_2O content.

REGRESSION AND THERMODYNAMIC MODELS

To improve the reliability of the OSAT for natural samples, we here develop a thermodynamic formalism for Al exchange between olivine and spinel and two empirical regression models. We applied a Monte Carlo cross-validation (MCCV; e.g. Xu & Liang, 2001) algorithm to estimate the uncertainties of regression models.

Regression strategy and models

In our regression models, we first split the experimental data set into a training data set ($n = 95$) used for regression and a test data set including 21 experiments not included in the calibration to test the accuracy of the regression (details of training and test data set are given in the supplementary data set, Tables S2, 3). The standard error estimation (SEE) on the training data set and RMSE on the test data set were calculated accordingly. Then, to assess model uncertainties and eliminate sampling bias, we used a MCCV algorithm. In each calculation, we randomly divided the experimental data set into a 5:1 ratio of training and test data sets, and then performed 10-fold cross-validation on the training data set to estimate SEE_{MCCV} on the training data set and then $RMSE_{MCCV}$ on the test data set, which is also the recommended error on the thermometric model. Detailed information on the training and test data sets, as well as the MCCV results, are given in the Supplementary data (Tables S2 and S3; Section 3).

Thermodynamic formalism

To better understand the Al exchange between olivine and spinel, we here follow a thermodynamic formalism. Coogan et al. (2014)

argued that the most plausible mechanism for incorporating Al into olivine in a Cr-spinel-bearing system is:

$$\left(MgAl^{TET}\right)Al^{OCT}O_4^{Spl} = \left(MgAl^{TET}\right)Al^{OCT}O_4^{Ol} \tag{2}$$

which we follow in our thermodynamic framework (see details in Appendix A). For simplicity, in the following we assume thermodynamic ideality in the incorporation of Al in olivine, i.e. the excess energy caused from site ordering of Al is negligible. This assumption is based on the following considerations: 1) trace element incorporation is usually considered as a dilution so the internal energy can be calculated as a simplified pure component (Ganguly, 2008); 2) to the best of the authors' knowledge, there are currently no established models to accurately differentiate or calculate the coordination of different Al species in olivine and no calibration for the interaction parameters between sites. Al may also coordinate with a vacant site (Jollands et al., 2018; Shea et al., 2019; Lang et al., 2022); 3) established thermodynamic models for other trace elements in olivine (e.g. Ni) with similar assumption of ideality have shown a minimal influence on the internal energy (e.g. Matzen et al., 2013). We therefore believe our thermodynamic framework remains valid with this assumption. Al substitution in spinel is however more complicated due to its high Al abundance, site ordering, and the known non-ideal mixing behavior of spinel components. We apply the thermodynamic framework of Sack (1982) and Sack & Ghiorso (1991a, 1991b), and express the internal energy of spinel by five independent compositional variables (X_i) (see details in Appendix A; Sack & Ghiorso, 1991b).

After organizing the thermodynamic framework, olivine–spinel Al exchange can be described as (see Appendix A):

$$\ln\left(\frac{X_{Al_2O_3^{Ol}}}{X_{Mg^{2+}}^{TET} X_{Al^{3+}}^{OCT}}\right) + b = \frac{\varphi^{Spl}}{c_0 \times T} \tag{3}$$

which can be rearranged as:

$$T = \frac{\varphi^{Spl}}{c_0 \times \left(\ln\left(\frac{X_{Al_2O_3^{Ol}}}{X_{Mg^{2+}}^{TET} X_{Al^{3+}}^{OCT}}\right) + b\right)} \tag{4}$$

where:

$$\varphi^{Spl} = c_1 X_2 + c_2 X_2^2 + c_3 X_2^{\frac{1}{2}}$$

$$+ c_4 \left(1 - X_2\right)\left(1 + X_4 - X_2\right)$$

$$+ c_5 \left(1 - X_2\right)(X_3) + c_6 \left(1 - X_2\right)(X_4) + c_7 \left(1 - X_2\right)(X_5)$$

$$+ c_8 X_3 \left(X_3 + X_4 + X_5\right)$$

$$+ c_9 X_4 \left(X_3 + X_4 + X_5\right)$$

$$+ c_{10} X_5 \left(X_3 + X_4 + X_5\right)$$

$$- c_{11} (X_3)(X_4) - c_{12} (X_3)(X_5) - c_{13} (X_4)(X_5) + c_{14}$$

Here, R is the gas constant (8.314 J mol^{-1} K^{-1}), $X_{Mg^{2+}}^{TET}$ is the mole fraction of Mg in the spinel tetrahedral site, $X_{Al^{3+}}^{OCT}$ is the mole fraction of Al in the spinel octahedral site, and T is temperature in Kelvin. In Eq. 4, X_i are independent compositional variables used to describe spinel composition (Si, Ti, Fe, Mg, Cr, Al, and Mn; Sack & Ghiorso, 1991b); they are listed in Table A1. Other parameters (b, c_0–c_{14}) are regression coefficients fitted to the experimental data set through a polynomial curve-fitting approach. In Eq. 3, because
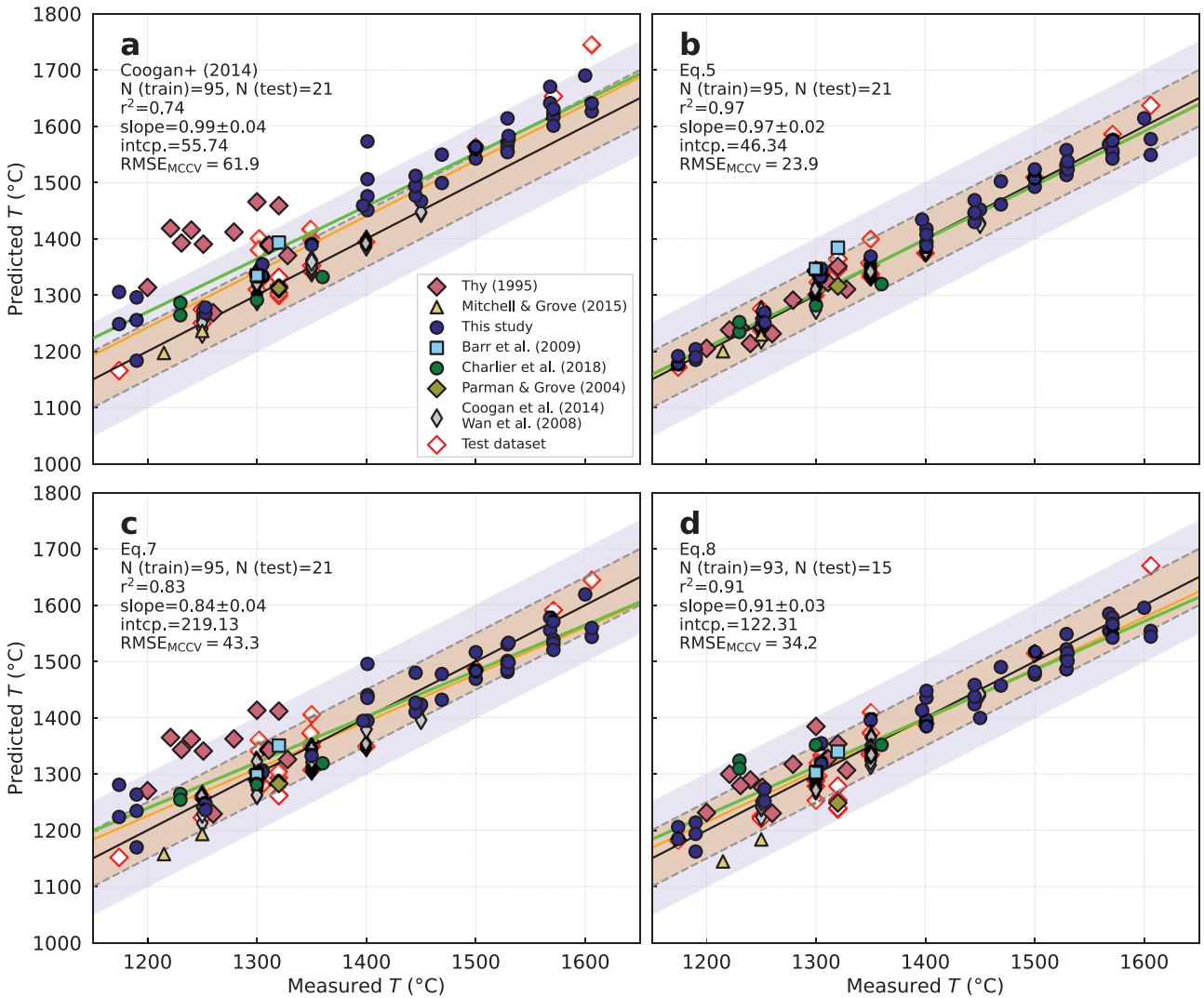
Fig. 5. Comparison of crystallization temperatures calculated using **(a)** the model of Coogan *et al.* (2014) and **(b–d)** Eqs. 5, 7, and 8, respectively. The green line represents the results of a Monte Carlo simulation showing the robustness of the fit when 1σ standard errors on spinel and olivine compositions are considered. The r^2 values represent the robustness of the linear regressions between the measured temperatures and predicted temperatures. The brown and purple fields represent temperatures within $\pm50°C$ and $\pm100°C$. Data sources as in Fig. 1.

the term $X_{Mg^{2+}}^{TET} X_{Al^{3+}}^{OCT}$ is proportional to spinel Al_2O_3 content, we can simplify the equation by replacing the $\ln\left(\frac{X_{Al_2O_3}^{Ol}}{X_{Mg^{2+}}^{TET} X_{Al^{3+}}^{OCT}}\right)$ with $\ln K_{DAl}$. The final regression on the training data set is:

$$T\,(K) = \frac{10,000 \times \varphi^{Spl}}{-0.168 \times \left(\ln K_{DAl} + 0.654\right)} \quad (5)$$

where

$$\varphi^{Spl} = 1.487X_2 - 0.593X_2^2 - 0.630X_2^{\frac{1}{2}}$$

$$+0.390\left(1 - X_2\right)\left(1 + X_4 - X_2\right)$$

$$+0.009\left(1 - X_2\right)\left(X_3\right) - 2.492\left(1 - X_2\right)\left(X_4\right) + 0.065\left(1 - X_2\right)\left(X_5\right)$$

$$-0.031X_3\left(X_3 + X_4 + X_5\right)$$

$$-4.141X_4\left(X_3 + X_4 + X_5\right)$$

$$-0.428X_5\left(X_3 + X_4 + X_5\right)$$

$$+4.637\left(X_3\right)\left(X_4\right) + 0.054\left(X_3\right)\left(X_5\right) + 10.803\left(X_4\right)\left(X_5\right) + 2.714 \quad (6)$$

The regression result for Eq. 5 is shown in Fig. 5b and Table A2: the SEE and r^2 values for the training data set are $\pm20.2°C$ and 0.97, respectively, RMSE on the test data set is 29.0°C, and the P value of the fit, where a no correlation alternative null hypothesis being tested against, is 1.11e−16. The MCCV result shows that the median SEE$_{MCCV}$ and r^2_{MCCV} values for the training data set are 20.2°C and 0.97, respectively, and the median RMSE$_{MCCV}$ value for the test data set is ∼23.9°C.

Empirical expressions

By using our expanded experimental data set, we first recalibrated an empirical model similar to the regression format of Coogan *et al.* (2014) but with unweighted multiple linear regression (see supplementary material for a comparison with a weighted regression method, Section 4):

$$T\,(K) = \frac{10,000}{0.740(0.317) + 1.144(0.136)\mathbf{Cr\#} - 0.865(0.046)\ln K_{DAl}} \quad (7)$$

The regression result of this new thermometer is shown in Fig. 5c and Table A2: the SEE and r^2 values for the training data
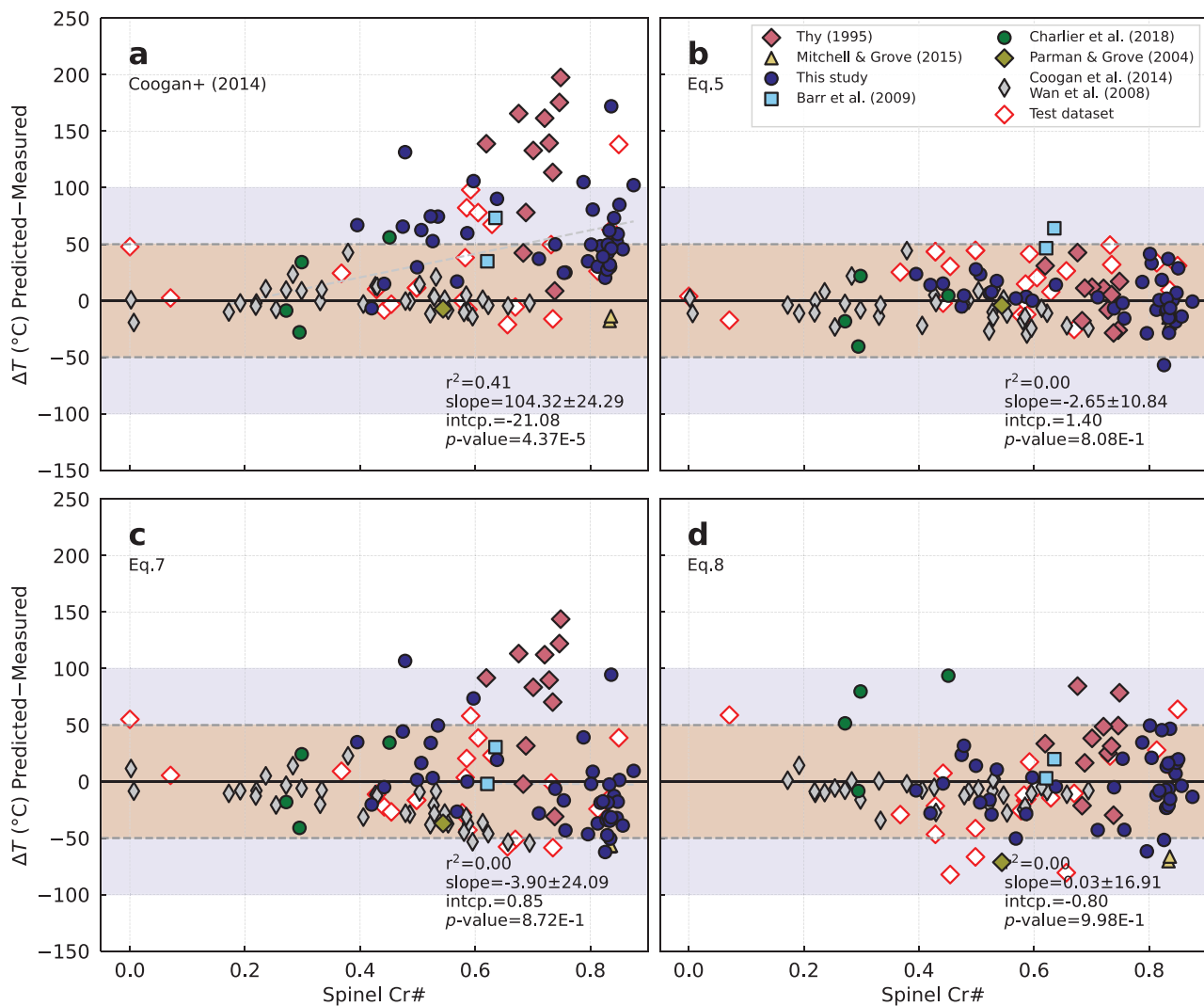
Fig. 6. Effects of spinel Cr# on **(a)** the OSAT of Coogan *et al.* (2014) and **(b–d)** the extended OSAT using Eqs. 5, 7, and 8, respectively. Data sources as in Fig. 1.

set are ±44.8°C and 0.83, respectively, RMSE on the test data set is 34.4°C, and the *P* value of the fit is 2.88e−36. The MCCV result shows that the median SEE_{MCCV} and r^2_{MCCV} values for the training data set are 42.1°C and 0.92°C, respectively, and the median $RMSE_{MCCV}$ value for the test data set is 43.3°C.

Considering that Cr may have a coupled substitution with Al when entering olivine to form a $(MgAl)Cr_2O_4$ structure (Hanson & Jones, 1998; Milman-Barris *et al.*, 2008; Jollands *et al.*, 2018), we explored whether the Cr exchange between olivine and spinel (K_{DCr}) would improve the empirical thermometric equation:

$$T\ (K) = \frac{10,000}{\begin{array}{l}0.049(0.241) - 0.657(0.040)\ln K_{DAl}\\ -0.389(0.041)\ln K_{DCr} + 0.543(0.121)\mathbf{Cr\#}\end{array}} \quad (8)$$

Cr-free experiments were excluded during regression (Fig. 5d and Table A2). The SEE and r^2 values for the training data set are ±31.7°C and 0.91°C, respectively, RMSE on the test data set is 39.1°C, and the *P* value of the fit is 3.79e−47. The MCCV result shows that the SEE_{MCCV} and r^2_{MCCV} values for the training data set are 35.8°C and 0.94°C, respectively, and the median $RMSE_{MCCV}$

value for the test data set is 34.2°C. We are aware that Eq. 8 includes all the regression variables from Eq. 7. To determine if the improved performance of Eq. 8 is due to more regression terms or statistical significance, we performed a *F*-test (see Appendix B for further details on the *F*-test model). The results of the *F*-test show an *F* score of 88.4 and a *P* value of 5.4e−15, which is statistically significant ($P < 0.05$) at 95% confidence. Therefore, the incorporation of Cr exchange as K_{DCr} into Eq. 8 produced a statistically superior fit compared to Eq. 7.

FACTORS AFFECTING THE PERFORMANCE OF THE MODELS
Dependence of the models on spinel composition and olivine–spinel Cr exchange
Previous studies have noted limitations of the original thermometric calibration due to the restricted range of Cr# values used in the calibration (e.g. Heinonen *et al.,* 2015; Xu & Liu, 2016; Trela *et al., 2017*). In Fig. 6, we compare spinel Cr# with the ΔT calculated using our three new models and that of Coogan *et al.* (2014). There is no apparent correlation between ΔT and spinel Cr# calculated using Eqs. 5, 7, and 8, whereas the model of Coogan *et al.* (2014)
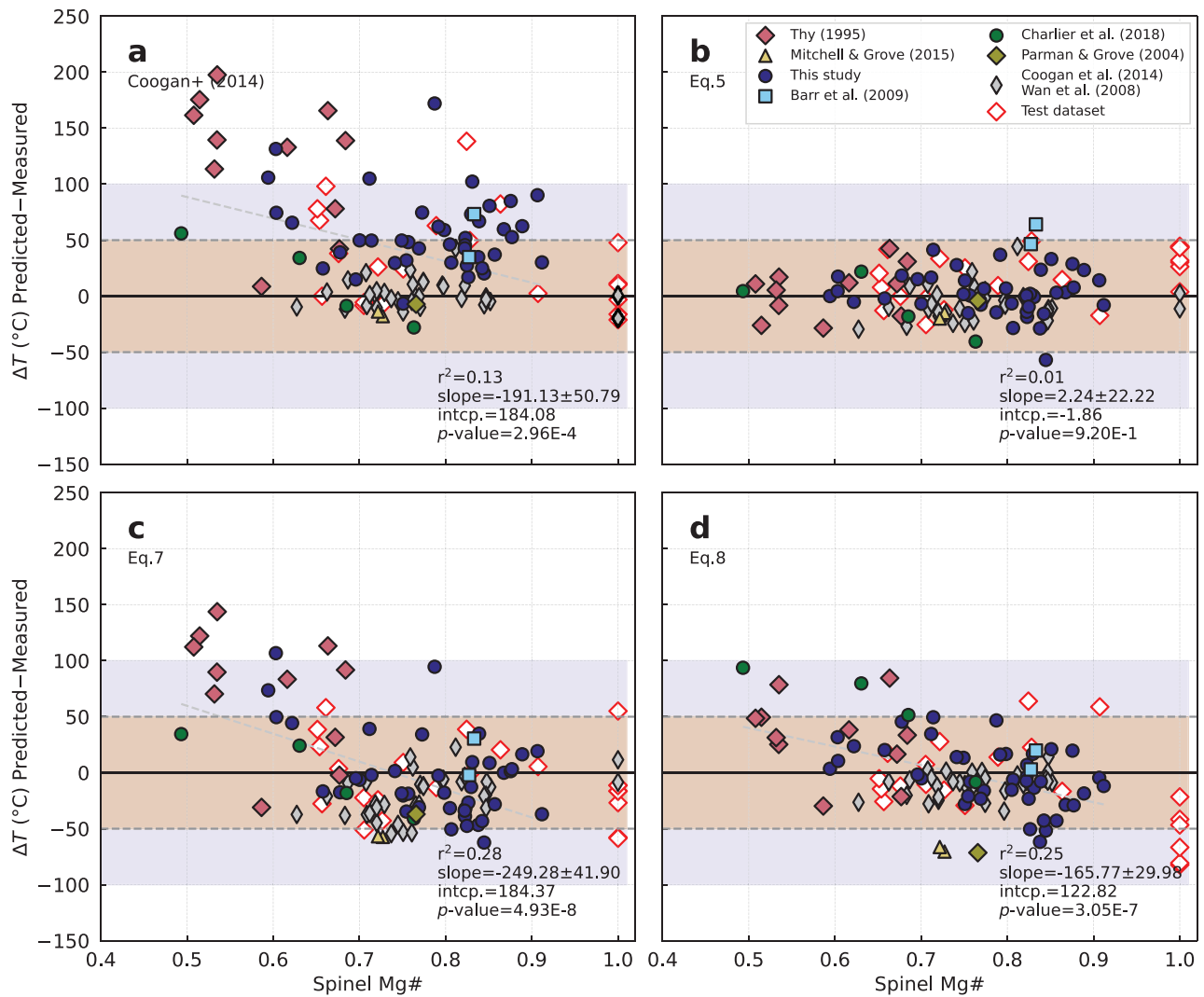
Fig. 7. Effects of spinel Mg# on **(a)** the OSAT of Coogan et al. (2014) and **(b–d)** the extended OSAT using Eqs. 5, 7, and 8, respectively. Data sources as in Fig. 1.

shows a moderate correlation ($r^2 = 0.41$). Spinel Fe^{3+}/Fe^{2+} has a moderate impact on ΔT using the model of Coogan et al. ($r^2 = 0.47$), a limited impact using Eq. 7 ($r^2 = 0.24$), and negligible impacts on on Eqs. 5 and 8 (Fig. S6). The effect of spinel TiO_2 content was negligible for all models (Fig. S7).

Spinel Mg# and $Fe^{3+}/(Fe^{3+} + Cr + Al)$ affect the performance of Eq. 7 ($r^2 = 0.28$ and 0.66, respectively) and the model of Coogan et al. (2014; $r^2 = 0.13$ and 0.76, respectively), but have less effect on Eqs. 5 and 8 (Figs. 7, 8). Similarly, K_{DCr} has a moderate effect on Eq. 7 and the model of Coogan et al. (2014), but not on Eqs. 5 and 8, suggesting that K_{DCr} is indeed an important parameter for improving the accuracy of the empirical models (Fig. S8). The thermodynamic model Eq. 5 including the spinel composition, may also mimic the effect of K_{DCr}. The correlation of ΔT with the spinel compositional parameters and K_{DCr} indicates that using only spinel Cr# and K_{DAl} is not sufficient to accurately predict temperature in all circumstances, particularly when spinel has a low Mg# or high $Fe^{3+}/(Fe^{3+} + Cr + Al)$ as is often observed in natural LIP spinels (Fig. 1). In such cases, the model of Coogan et al. (2014) and Eq. 7 may have larger uncertainties and may strongly overestimate temperature.

Dependence of the thermometers on fO_2, H_2O, and pressure

fO_2 does not strongly affect the accuracy of the temperature calibrations of any of the models, but a weak negative correlation was observed for Eq. 8 (Fig. S9). We further tested the effect of melt water content and pressure with our reanalyzed experimental data set (three hydrous experiments with 3.7–7.4 wt % H_2O in the experimental glass; seven dry high-pressure experiments at 500–1350 MPa). Although water is known to have a profound effect on the olivine liquidus (Médard & Grove, 2008), this appears to be of negligible consequence on the accuracy of any of the thermometric models (Fig. S10). A potential explanation of this is that the effect of water is compensated by changes to the olivine and spinel compositions. Pressure, however, shows a moderate correlation in all models, although the results are within the uncertainty of each model (Fig. 9). It is unclear whether this correlation is due to sample bias related to the sparse high pressure experiments, or if pressure may affect on the molar volume of spinel and site occupancy (Hamecher et al., 2013). Nonetheless, D'Souza et al. (2020) proposed that pressure has no effect on the model of Coogan et al. (2014).
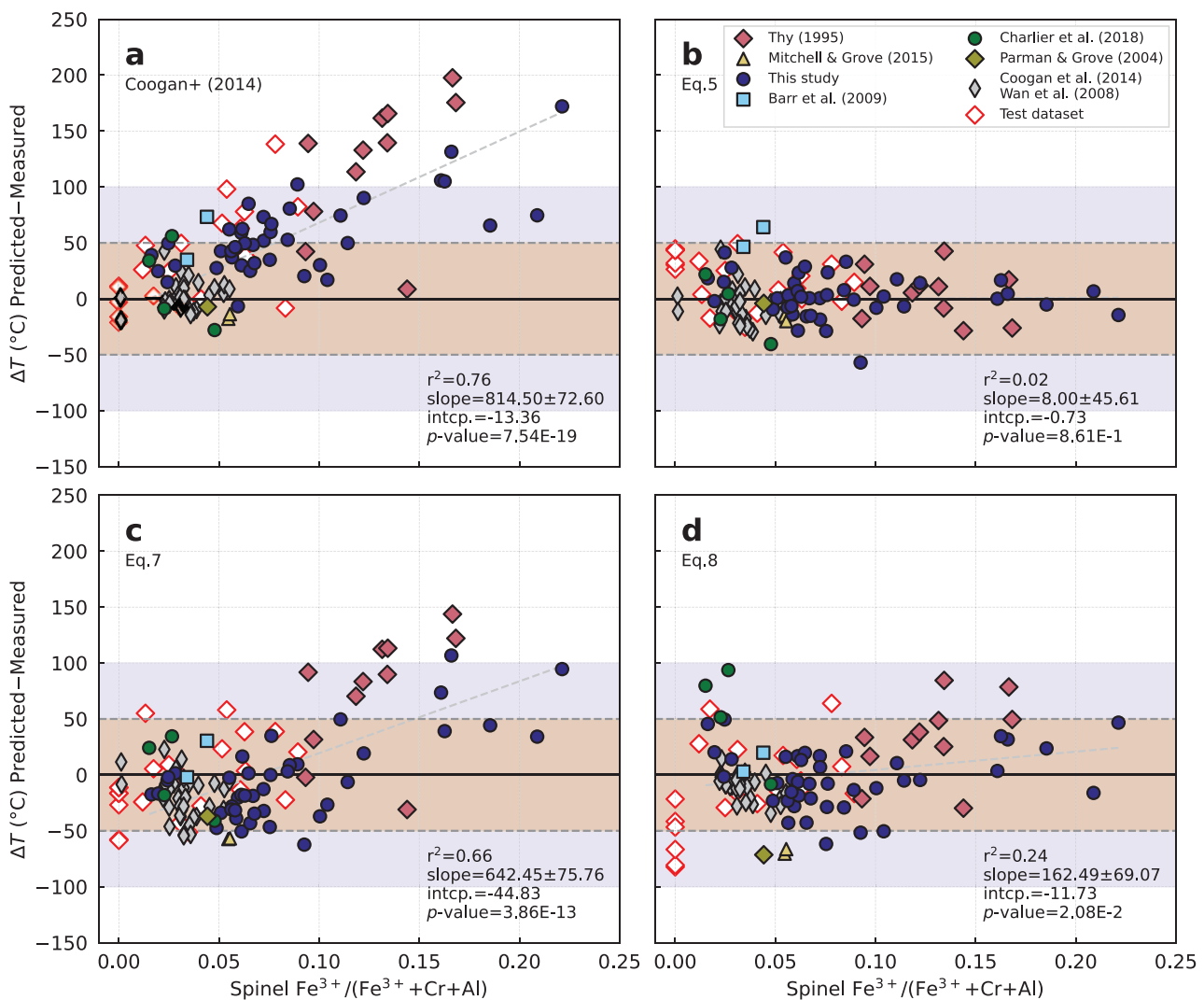
Fig. 8. Effects of spinel $Fe^{3+}/(Fe^{3+} + Cr + Al)$ on **(a)** the OSAT of Coogan *et al.* (2014) and **(b–d)** the extended OSAT using Eqs. 5, 7, and 8, respectively. Data sources as in Fig. 1.

DISCUSSION

In this section, we discuss the limits of the thermometric models and their sensitivities to subsolidus re-equilibration. We then establish a protocol for selecting the appropriate model for applications to natural samples. Finally, we apply our models to constrain mantle melting conditions and lithological components in a range of geological settings and use thermodynamic calculations to assess potential re-equilibration in natural olivine-spinel pairs.

Concerns, limits, and sensitivities of the models

Our thermodynamic model (Eq. 5) is accurate but involves the exchange of Fe and Mg, which diffuse rapidly in spinel (Vogt *et al.*, 2015). This means that temperature estimates in natural systems could be affected by low-temperature re-equilibration due to olivine-spinel subsolidus Fe–Mg exchange during cooling. We note that the system itself doesn't have be subsolidus, i.e. the olivine-spinel pair could crystallize at high temperature but experienced a Fe–Mg reset after being carried along in an evolved melt, or set in a partially molten mush before re-entrainment and eruption. The empirical model Eq. 8 does not involve Fe and Mg but incorporates Cr exchange between olivine and spinel. Subsolidus Cr

re-equilibration in olivine, potentially caused by Cr reset between the carrier liquid, could also result in Eq. 8 potentially yielding anomalously low temperature estimates, we however note that the diffusivity of Cr in olivine is poorly constrained and may vary with fO_2 and Cr concentrations in olivine (Ito & Ganguly, 2006; Jollands *et al.*, 2018). In contrast, the empirical models of Eq. 7 and Coogan *et al.* (2014) only involve slow diffusive elements in spinel and olivine (Spandler & O'Neill, 2010; Vogt *et al.*, 2015). Therefore, they are not impacted by low-temperature re-equilibration, but tend to overestimate temperature when spinel has low Mg# or high $Fe^{3+}/(Fe^{3+} + Al^{3+} + Cr^{3+})$ (Figs. 7 and 8).

To quantitatively investigate the sensitivities of Eq. 5 to Fe–Mg re-equilibration and Eq. 8 to Cr re-equilibration in olivine, we performed two numerical simulations: 1) we modeled Fe–Mg re-equilibration in a stoichiometric Cr-spinel with the formula $(Mg, Fe^{2+})(Al, Cr, Fe^{3+})_2O_4$, and 2) we progressively added Cr_2O_3 to olivine to model Cr re-equilibration. In the Fe–Mg re-equilibration model, Al diffusivity in olivine is slow (Spandler & O'Neill, 2010), so we assumed that spinel exchanges only Fe^{2+} and Mg with olivine and, therefore, the spinel Cr# remains constant at a fixed fO_2, which is consistent with natural observations (Guo *et al.*, 2009; Hu *et al.*, 2022). Spinel Mg# were set to values vary from 0.3 to 1 with an increment of 0.01 at each spinel Cr#, which we varied from 0.4 to
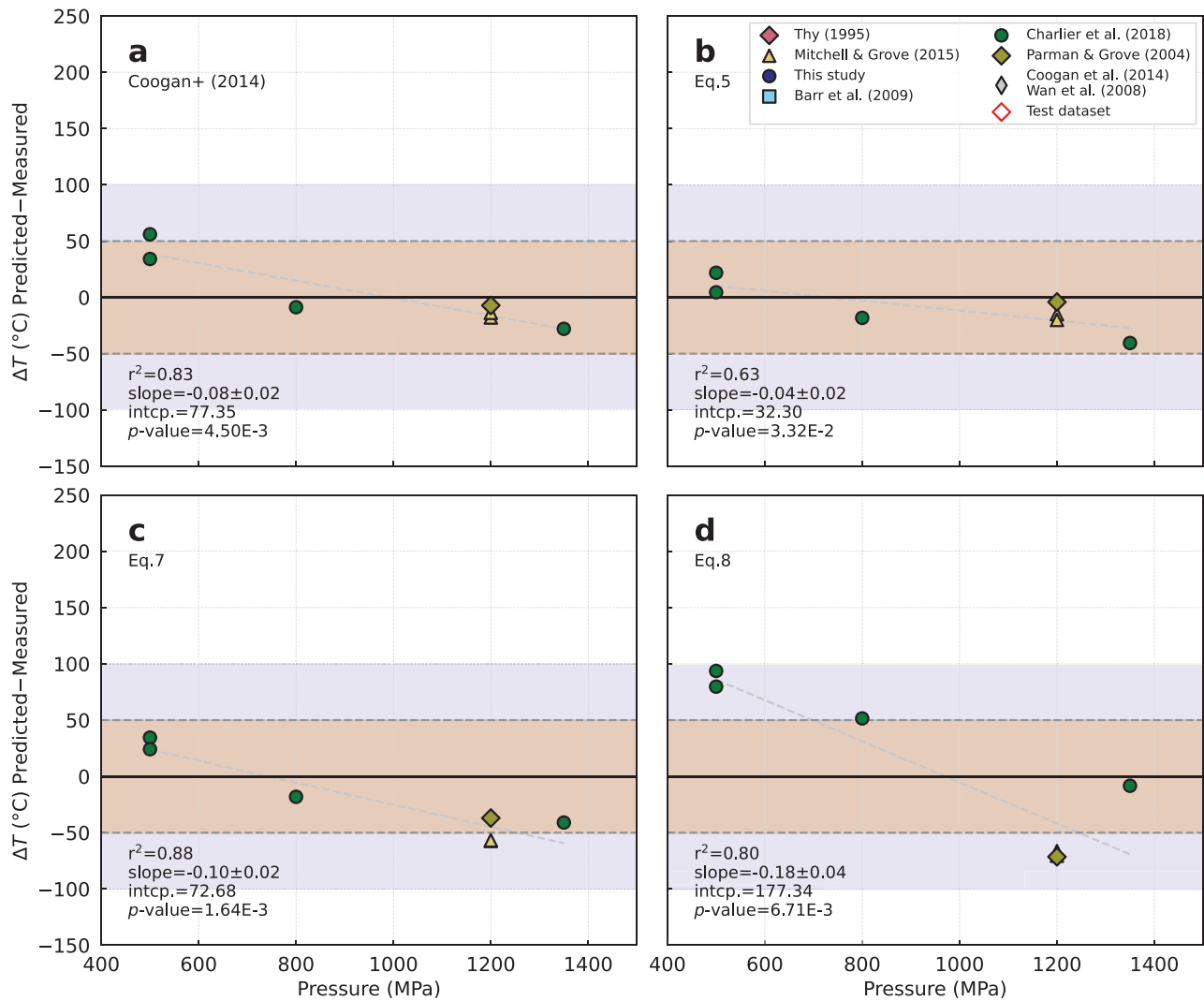
Fig. 9. Effects of pressure (MPa) on **(a)** the OSAT of Coogan *et al.* (2014) and **(b–d)** the extended OSAT using Eqs. 5, 7, and 8, respectively. Data sources as in Fig. 1.

0.9 with the same increment to cover the whole range observed in nature. We held spinel Fe^{3+}/Fe^{2+} constant at 0.5, corresponding to the median of natural spinel compositions, Olivine Al_2O_3 content was set to 500 μg/g. Temperatures were then calculated using Eq. 5. Because the mechanism of Cr re-equilibration in olivine has not been well determined (Milman-Barris *et al.*, 2008; Shea *et al.*, 2019; Lang *et al.*, 2022), we modeled two scenarios. In the first scenario we assumed a decoupled substitution between Cr and Al, i.e. the Cr content changes but the Al content remains constant, consistent with our experimental observation. In the second scenario, we assumed coupled substitution of Cr and Al with a molar ratio of 1, similar to the observations of Milman-Barris *et al.* (2008) in a fast growth regime. Both scenarios olivine Cr_2O_3 start from 200 to 1500 μg/g. Olivine Al_2O_3 content was set to 500 μg/g in the first scenario and range from 134 to 1006 μg/g in the second scenario, holding molar Cr/Al = 1. Temperatures were then calculated using Eq. 8.

Our model results are shown in Fig. 10. Decreasing spinel Mg# and decreasing olivine Cr_2O_3 content (both decoupled and coupled substitutions) return lower temperatures when using Eqs. 5 and 8, respectively. For a given degree of Fe–Mg or Cr re-equilibration, the decrease in apparent temperature after a given degree of re-equilibration is greater for spinel with higher Cr#,

whereas Eq. 5 tends to underestimate temperature for spinel with lower Mg#.

Selecting the appropriate model for application to natural samples

The reliability of the empirical model in Eq. 7 is limited to a specific range of spinel compositions and has larger errors on the temperature estimation compared to the thermodynamic model Eq. 5 and the empirical model Eq. 8. In contrast, Eqs. 5 and 8 are more precise but may be affected by chemical re-equilibration, as discussed above. Given the greater uncertainties in the empirical expressions (Eqs. 7 and 8), for a fully equili-brated, primitive olivine-spinel pair, we expect them to return temperatures scattering above and below that returned by the thermodynamic expression (Eq. 5). In turn, we expect Eq. 5 to return lower temperatures than the Eqs. 7 and 8 if diffusive re-equilibration occurs. Therefore, we consider that Eqs. 7 or 8 should be used when Eq. 5 has a more than 50% chance of underesti-mating the true temperature (i.e. when the mean temperatures estimated using Eq. 5 and either Eq. 7 or 8 differ sufficiently that a P value test on the distributions having the same mean returns $P < 0.5$). Model selection is then determined by the likelihood that Eq. 5 yields an underestimation. If the temperature estimated
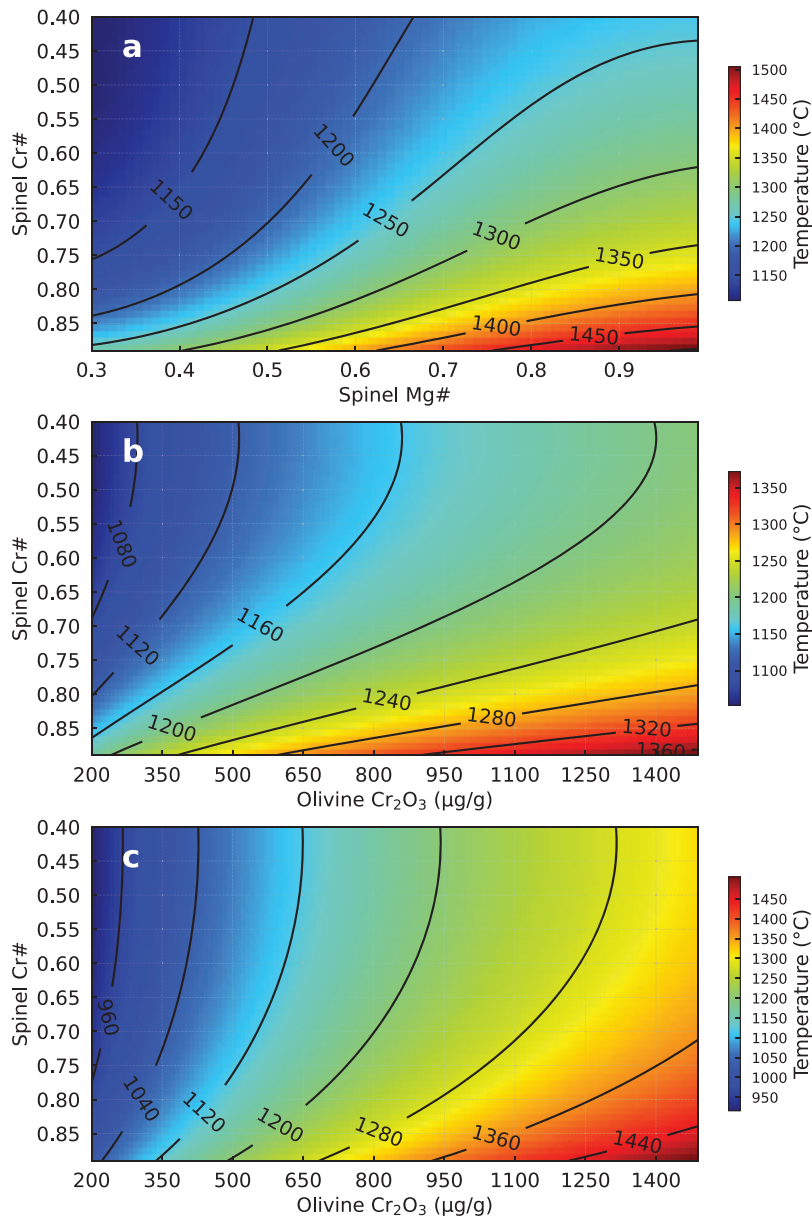
Fig. 10. Modeled effects of **(a)** Fe–Mg re-equilibration in spinel on temperatures estimated using Eq. 5 and **(b)** Cr re-equilibration (decoupled substitution) in olivine on temperatures estimated using Eq 8. **(c)** Cr re-equilibration (coupled substitution with Al) in olivine on temperatures estimated using Eq 8.

using Eq. 5 is higher than that estimated using Eq. 7 or 8, the result from the thermodynamic expression should be chosen. If not, a statistical Z-test is introduced to decide whether to choose the thermodynamic expression or empirical expression (e.g. Snedecor & Cochran, 1989):

$$Z = \frac{|T_i - T_j|}{\sqrt{\sigma_{X_i}^2 + \sigma_{X_j}^2}} \qquad (9)$$

where σ_{X_i} and σ_{X_j} are the RMSEs of the two models being compared (Eqs. 5 vs. Eq. 7 and/or Eq. 8) and T_i and T_j are the respective temperature estimates. If $Z > 1.35$, there is a 50% chance that the two temperatures differ by a value larger than that attributed to their combined uncertainties, and that Eqs. 7 or 8 return a higher temperature which is closer to the true value. If both Eqs. 7 and 8 are compared with Eq. 5, the pair that yields with the higher Z score should be chosen to obtain a larger probability that the

temperature estimates are different from each other. The Z value of 1.35 represents a width of 1.35 standard deviations, which is required for 50% of normal distributions with standard deviations given by each model to lie between the mean $-\frac{1}{2}|T_i - T_j|$ and the mean $+\frac{1}{2}|T_i - T_j|$ (i and j represent each thermometric model); i.e. when $Z < 1.35$, 50% of the estimated temperatures should be more similar if they are measuring the same temperature. A python script and an Excel spreadsheet to perform all relevant calculations can be found at https://github.com/eazzzon/olspthermo). Table 3 lists all scenarios for selecting the appropriate model.

To illustrate the use of the protocol outlined above, we provide two geological examples. In the first example, we take an ocean island basalt from Pico Island (Azores, Portugal) containing a Fo$_{83}$ olivine crystal, which has two spinel inclusions (van Gerve et al., 2021). X-ray chemical maps show no Al, Cr, or P zoning in the olivine and stable Al concentration profiles were acquired from

Table 3: Scenarios for selecting the appropriate model for OSAT

Scenarios	Model selection
Compare 3 models (Eq. 5, Eq. 7 & Eq. 8)	
S1: T_Eq5 > T_Eq7, T_Eq5 > T_Eq8	Eq.5
If not S1, apply Z-test:	
Z_(Eq5&Eq7) > Z_(Eq5&Eq8) > 1.35	Eq.7
Z_(Eq5&Eq8) > Z_(Eq5&Eq7) > 1.35	Eq.8
Z_(Eq5&Eq8) < 1.35, Z_(Eq5&Eq7) < 1.35	Eq.5
Z_(Eq5&Eq7) > 1.35 > Z_(Eq5&Eq8)	Eq.7
Z_(Eq5&Eq8) > 1.35 > Z_(Eq5&Eq7)	Eq.8
Compare 2 models (Eq. 5 & Eq. 7)	
S2: T_Eq5 > T_Eq7	Eq.5
If not S2, apply Z-test:	
Z_(Eq5&Eq7) > 1.35	Eq.7
Z_(Eq5&Eq7) < 1.35	Eq.5

the olivine till approaching the spinel-olivine boundaries (see in the Supplementary material, Section 5). The spinel inclusions have Mg# ≈ 0.51 and $Fe^{3+}/(Fe^{3+} + Cr + Al) \approx 0.17$. The temperatures calculated using Eqs. 5, 7, and 8 are $1091 \pm 23°C$, $1171 \pm 43°C$, and $1184 \pm 34°C$, respectively, with errors propagated from both analytical and thermometric uncertainties. Because the thermodynamic expression returns a lower temperature than the empirical expressions, we applied the Z-test model. The results show $Z = 1.62$ between Eqs. 5, and 7 and $Z = 0.76$ between Eqs. 5 and 8. Because of the larger Z-score, the result from Eq. 7 is statistically more robust, which is consistent with the temperature estimated from a melt inclusion within the same crystal using liquid thermometry ($\sim 1194 \pm 46°C$; van Gerve et al., 2021) and previous experimental studies (e.g. Grove et al., 1992; Toplis & Carroll, 1995). According to these results, Eq. 5 significantly underestimates the temperature by $\sim 80°C$.

For our second example, we take four published analyses of a MORB sample (A25-D20–8) from Coogan et al. (2014), which contains an Fo_{91} olivine and a spinel with Mg# = 0.81. Eqs. 5, 7, and 8 return temperatures of $1265 \pm 23°C$, $1235 \pm 43°C$, and $1198 \pm 34°C$, respectively. Here, the thermodynamic expression is chosen because it returns a higher temperature than the empirical expressions, hence the recommended temperature is $1265 \pm 23°C$.

Application of the extended OSAT to natural basalts

Here, we apply our new thermometers to basalts from various settings: the Siqueiros MOR, Iceland and Skye in the North Atlantic igneous province (NAIP), and the Emeishan, Etendeka, and Caribbean LIPs. The results of different models are shown in Table 4 and Fig. 11. In each case, and for each analysis, we chose results according to the Z-test protocol described above. For comparison, all temperature estimates from each model are shown in Fig. S11. Given the similarity of spinel compositions from MORB, Iceland and Skye with those from experiments used in the previous calibration of Coogan et al. (2014) and Wan et al. (2008), the new temperature estimates from our models are comparable or fall within mutual uncertainties. Intra-plate igneous provinces generally have higher $Fe^{3+}/(Fe^{3+} + Cr + Al)$ and lower Mg# (Fig. 1), therefore the model of Coogan et al. (2014) significantly overestimate the temperature by 30–100°C (median) and 60–120°C at the maximum.

MORB (Siqueiros)

MORB lavas erupted at Siqueiros are generated by near-adiabatic upwelling of the ambient upper mantle (e.g. Gregg et al., 2009). Siqueiros spinel has Cr# = 0.24–0.44, and potentially experienced less Fe–Mg subsolidus re-equilibration, with generally high Mg# values (0.70–0.81) and $Fe^{3+}/(Fe^{3+} + Cr + Al)$ values (0.03–0.07). Olivine contains 335–827 $\mu g/g$ Al_2O_3 and 508–2750 $\mu g/g$ Cr_2O_3. Coogan et al. (2014) and Matthews et al. (2021) calculated the co-crystallization temperature of Siqueiros olivine and spinel to be 1230^{+59}_{-91} °C (expressed as $median^{+[95^{th}\ percentile - median]}_{-[median - 5^{th}\ percentile]}$, being consistent with the description of distribution used in Matthews et al. [2021]). Our new estimated temperatures are 1258^{+37}_{-76} °C. These new estimates generally agree with the previous studies, which we attribute to the spinel composition in Siqueiros lavas being comparable to those used in the calibration experiments of Coogan et al. (2014) and Wan et al. (2008).

NAIP (Iceland and Skye)

Iceland and Skye are within the NAIP, which is accepted as having a mantle-plume origin. Spinel in Iceland has Cr# 0.24–0.60, Mg# 0.54–0.79 and $Fe^{3+}/(Fe^{3+} + Cr + Al)$ 0–0.13. Olivine ins Iceland contain Al_2O_3 396–1020 $\mu g/g$ and Cr_2O_3 345–2686 $\mu g/g$. Spinel in Skye is slightly more primitive, containing Cr# 0.41–0.56, Mg# 0.70–0.77 and $Fe^{3+}/(Fe^{3+} + Cr + Al)$ 0.03–0.06. Olivine in Skye has more Al_2O_3 (794–1519 $\mu g/g$) and less Cr_2O_3 (1030–1890 $\mu g/g$). Previous crystallization temperature estimates (Matthews et al., 2016; Spice et al., 2016) using the model of Coogan et al. (2014) gave crystallization temperatures of 1283^{+84}_{-66} °C for Iceland and 1409^{+60}_{-65} °C for Skye. Our new results are 1275^{+52}_{-100} °C for Iceland and 1388^{+41}_{-53} °C for Skye, which are similar on the median values but $\sim 40°C$ lower for the high temperature populations (on the 95th)

Emeishan large igneous province

The ~ 260 Ma Emeishan LIP in southwest China is considered to be of mantle-plume origin (Chung & Jahn, 1995; Xu et al., 2001; Xiao et al., 2004). Emeishan spinel compositions are much more varied compared to MORB, with Cr# = 0.42–0.72, Mg# = 0.48–0.72, and $Fe^{3+}/(Fe^{3+} + Cr + Al)$ = 0.04–0.15. Olivine contains 340–990 $\mu g/g$ Al_2O_3 and 165–1420 $\mu g/g$ Cr_2O_3. Previous temperature estimates give a crystallization temperature of 1271^{+108}_{-55} °C (Xu & Liu, 2016). Our new estimate is 1224^{+109}_{-54} °C, with both the median and 95th value being $\sim 47°C$ cooler. Here, the compositional deviation of the natural olivine and spinel from those used in the previous calibration results in the overestimated crystallization temperatures.

Etendeka large igneous province

The Etendeka LIP is the southern part of Paraná-Etendeka LIP, mainly outcropping in Namibia and southern Angola (Thompson et al., 2001; Gibson, 2002). The high crystallization temperatures and high $^3He/^4He$ values (>26 R_A, reported relative to that of the present-day atmosphere) of the lavas suggest a mantle plume origin (Stroncik et al., 2017). Etendeka spinel compositions are quite variable, with Cr# = 0.40–0.70, Mg# = 0.24–0.76, and $Fe^{3+}/(Fe^{3+} + Al^{3+} + Cr^{3+})$ = 0.04–0.31. Olivine contains 300–1200 $\mu g/g$ Al_2O_3 and 200–2200 $\mu g/g$ Cr_2O_3. Jennings et al. (2019) calculated the olivine crystallization temperature using the model of Coogan et al. (2014) to be 1323^{+151}_{-101} °C. Our new results are 1307^{+110}_{-88} °C, which are similar at the median value but 57°C lower for the high temperature populations (on the 95th).

Table 4: Comparison of the temperature estimates of models

Location	observations	Eq. 5		Eq. 7		Eq. 8		Model of Coogan *et al.* (2014)	
		Min-Max (°C)	T_{cry} (°C)[a]	Min-Max (°C)	T_{cry} (°C)	Min-Max (°C)	T_{cry} (°C)	Min-Max (°C)	T_{cry} (°C)
MORB (Siqueiros)	22	1167–1296	1250^{+45}_{-71}	1096–1260	1197^{+63}_{-84}	1115–1278	1218^{+57}_{-85}	1121–1292	1230^{+59}_{-91}
Iceland	85	1145–1362	1274^{+50}_{-100}	1112–1350	1247^{+87}_{-89}	1169–1345	1264^{+68}_{-63}	1183–1383	1283^{+84}_{-66}
Skye	35	1315–1436	1388^{+41}_{-53}	1290–1425	1348^{+45}_{-45}	1307–1436	1376^{+55}_{-59}	1337–1474	1409^{+60}_{-65}
Emeishan	48	1131–1391	1202^{+130}_{-60}	1061–1361	1145^{+148}_{-69}	1166–1397	1238^{+98}_{-47}	1188–1439	1271^{+108}_{-55}
Etendeka	62	926–1420	1178^{+234}_{-146}	1157–1447	1268^{+153}_{-91}	1178–1455	1295^{+151}_{-89}	1197–1508	1323^{+151}_{-101}
Tortugal	157	1109–1506	1405^{+87}_{-194}	1191–1471	1389^{+62}_{-141}	1217–1522	1426^{+77}_{-150}	1250–1601	1492^{+89}_{-173}

[a]T_{cry} is reported as median value with 95th and 5th percentile quoted.

Caribbean large igneous province (Tortugal suite)

The Tortugal suite in Costa Rica is considered to be the product of the initial melting of the Galapagos plume in the Caribbean large igneous province (Alvarado *et al.*, 1997; Trela *et al.*, 2017). Particularly, the Tortugal suite hosts high-Fo olivine (up to Fo_{94}) with compositions overlapping those of olivine in Archaean komatiites and containing 321–1114 $\mu g/g$ Al_2O_3 and 807–2195 $\mu g/g$ Cr_2O_3. Tortugal suite spinel span a wide range of compositions, with Cr# = 0.66–0.85, Mg# = 0.33–0.72, and $Fe^{3+}/(Fe^{3+} + Cr+Al)$ = 0.0–0.14. Trela *et al.* (2017) used the model of Coogan *et al.* (2014) to estimate the crystallization temperature to be 1492^{+89}_{-173} °C. Our new estimates, however, are much lower, at 1425^{+77}_{-149} °C, which are 67°C lower on the median and 79°C lower for the high temperature populations (on the 95th).

Implications for mantle melting, mantle lithologies, and subsolidus re-equilibration

Significant overestimation of temperature is often observed when the model of Coogan *et al.* (2014) is applied to specific geological settings (e.g. intra-plate igneous provinces). This model was, however, abundantly used to assess mantle melting conditions and lithologies in those cases (e.g. Matthews *et al.*, 2016, 2021) which therefore necessitate a revision. Olivine crystallization temperatures can be converted to mantle T_p when a correction for the latent heat of melting is considered (Putirka *et al.*, 2007), which is directly related to the total melt fraction. The total melt fraction can be constrained from melting of a homogeneous (e.g. Putirka *et al.*, 2007) or a heterogenous mantle source (Matthews *et al.*, 2016, 2021), and through geophysical observations of magmatic productivity, i.e. crustal thickness at spreading centers or magma flux at ocean islands (McKenzie & Bickle, 1988; Shorttle *et al.*, 2014; Matthews *et al.*, 2016, 2021).

To be self-consistent with previous T_p and lithology estimates, we applied the protocol of Matthews *et al.* (2016, 2021) to estimate the mantle melting conditions and mantle lithologies for the localities investigated in this study. In this melting model, crustal thickness at oceanic spreading centers and magma flux at ocean islands are used as observable proxies for magma productivity. A multi-lithology mantle melting model during adiabatic decompression following Phipps Morgan (2001) and Shorttle *et al.* (2014) is used to calculate melting behavior. The source lithologies are assumed to be in thermal equilibrium. A full description of the mathematical and computational formulation is available in Phipps Morgan (2001) and Shorttle *et al.* (2014). An extra constraint was added to prevent negatively buoyant solution in intra-plate magmatism, i.e. the multi-lithology mantle should be buoyant with respect to the ambient mantle during the plume-driven upwelling. We used the python interface forward model pyMelt (version 1.96; Matthews *et al.*, 2022) to calculate the melting behavior of mantle compositions comprising multiple lithologies. The model considers three lithologies: lherzolite (*matthews.klb1* lithology class in pyMelt) and silica-deficient pyroxenite (*matthews.kg1* lithology class) from Matthews *et al.* (2021), and non-melting harzburgite (*shorttle.harzburgite* lithology class) from Shorttle *et al.* (2014).

To convert an observation of primary crystallization temperatures (T_{cry}) to the value of T_p, the fractions of mantle lithologies (ϕ_{Hz}, the harzburgite fraction; ϕ_{Px}, the pyroxenite fraction; and ϕ_{Lz}, the peridotite/lherzolite fraction), we used an inversion model of Matthews *et al.* (2021), a Bayesian Monte Carlo inference method (Feroz & Hobson, 2008; Feroz *et al.*, 2009, 2013; Buchner *et al.*, 2014) to find the set of solutions which can reproduce T_{cry} and mantle lithologies with applicable constraints (e.g. crustal thickness, magma flux). The inversion model parameters (lithospheric thickness, crustal thickness, the fraction of pyroxenite derived melt, magma flux) were kept identical to Table 1 in Matthews *et al.* (2021), also given in supplementary data set (Table S4), except for the T_{cry}, which we adapted to our new estimates above. We note that these parameters may not be the most appropriate for all our tested localities, but the focus here is on the influence of changing T_{cry} on mantle T_p and lithology estimates. The inversion model requires the selection of an appropriate olivine composition and crystallization temperature as the starting point of the calculation. Matthews *et al.* (2021) assumed Fo_{91} olivine as the composition equilibrated with primitive mantle-derived melts based on the most primitive olivine observed in nature. However, both experimental and natural observations (e.g. the Tortugal suite) have shown olivine of higher Fo ($>Fo_{94}$), indicating that the source diversity controls primary olivine compositions at different localities (see further discussion below). Here, we chose the maximum of our calculated T_{cry} estimates (the corresponding olivine Fo are close to or higher than 91) at each locality as the primary olivine temperature to simplify the constraints on the equilibrated olivine composition.

Our inversion results for T_p and mantle lithological fractions are summarized in Table 5 and shown in Fig. 12, details are given in the supplementary data set. Because different model parameters are used to constrain mantle T_p in different methods (e.g. Putirka, 2005, 2016), we only compare our new T_p values with those of Matthews *et al.* (2021) in Fig. 13 to be self-consistent.

Our new estimated T_p and lithology fractions (ϕ_{Hz} and ϕ_{Px}) for MORB (1355^{+24}_{-19}°C, $0.34^{+0.25}_{-0.30}$, and $0.02^{+0.02}_{-0.02}$, respectively), Iceland (1518^{+21}_{-17}°C, $0.23^{+0.18}_{-0.17}$, $0.08^{+0.04}_{-0.04}$), Skye (1550^{+80}_{-82}°C, $0.51^{+0.32}_{-0.39}$, $0.12^{+0.16}_{-0.10}$), and Etendeka (1577^{+106}_{-98}°C, $0.53^{+0.31}_{-0.38}$, $0.11^{+0.19}_{-0.10}$) are comparable to those of Matthews *et al.* (2021). However, due to previous
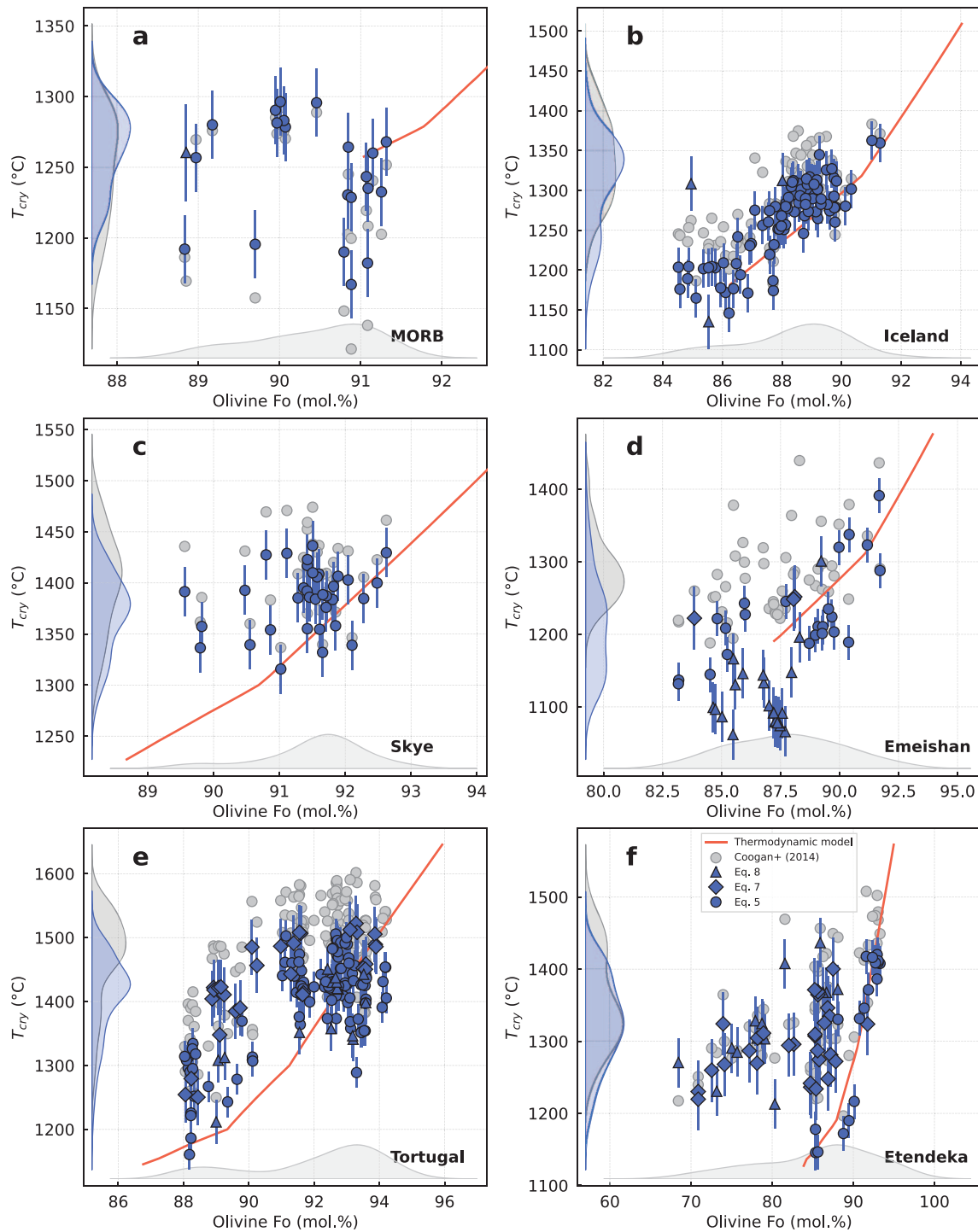
Fig. 11. Estimated crystallization temperatures for natural samples. Gray symbols are results using the model of Coogan *et al.* (2014). Blue symbols are results using the extended OSAT of this study that passed the Z-test protocol described in the text. Red lines are the calculated equilibrated olivine compositions and temperatures from our forward thermodynamic modeling using MAGEMin. See text for more details. The histograms along the left axis show compare the distribution of results using our model to those using the model of Coogan *et al.* (2014). The histogram along the bottom axis shows the distribution of olivine Fo contents, which is the same in both data sets.

overestimation of crystallization temperatures for intra-plate LIPs, our newly estimated T_p and lithological fractions differ significantly from Matthews *et al.* (2021). Our respective results for Emeishan (1481^{+87}_{-78}°C, $0.53^{+0.29}_{-0.36}$, $0.10^{+0.14}_{-0.09}$) return a median T_p that is 74°C cooler than previous inversions (Table 4), and our results for the Tortugal suite (1648^{+193}_{-91}°C, $0.50^{+0.31}_{-0.38}$, $0.15^{+0.29}_{-0.13}$) return a median T_p that is 165°C cooler, which leads to a remarkable difference in the estimated lithological fractions (Table 4).

To verify the reliability of the mantle melting and lithological estimates, we performed forward thermodynamic modeling based on the estimated mantle T_p and lithological fractions to calculate the equilibrated olivine composition in composition–temperature space. We used the Matlab/Julia Mineral Assemblages Gibbs Energy Minimization package (MAGEMin v1.3.0; Riel *et al.,* 2022) to calculate the equilibrium melt composition of a given mantle lithology under mantle melting conditions

Table 5: Summary of the posterior distributions of the T_p, ϕ_{Px}, ϕ_{Hz} in the inversion model as a comparison with the results from Matthews *et al.* (2021)

Location	T_{cry} (°C)[a]	This study			Matthews *et al.* (2021)		
		T_p (°C)	Φ_{Px}	Φ_{Hz}	T_p (°C)	Φ_{Px}	Φ_{Hz}
MORB	1266 ± 22	1355^{+24}_{-19}	$0.02^{+0.02}_{-0.02}$	$0.34^{+0.25}_{-0.30}$	1364^{+18}_{-23}	$0.02^{+0.02}_{-0.02}$	$0.40^{+0.16}_{-0.37}$
Iceland	1363 ± 24	1518^{+21}_{-17}	$0.08^{+0.04}_{-0.04}$	$0.23^{+0.18}_{-0.17}$	1525^{+21}_{-18}	$0.08^{+0.05}_{-0.04}$	$0.27^{+0.16}_{-0.20}$
Skye	1436 ± 24	1550^{+80}_{-82}	$0.12^{+0.16}_{-0.10}$	$0.51^{+0.32}_{-0.39}$	1566^{+73}_{-70}	$0.10^{+0.15}_{-0.10}$	$0.47^{+0.28}_{-0.39}$
Emeishan	1391 ± 24	1481^{+87}_{-78}	$0.10^{+0.14}_{-0.09}$	$0.53^{+0.29}_{-0.36}$	1555^{+100}_{-97}	$0.13^{+0.14}_{-0.10}$	$0.55^{+0.31}_{-0.38}$
Etendeka	1447 ± 34	1577^{+106}_{-98}	$0.11^{+0.19}_{-0.10}$	$0.53^{+0.31}_{-0.38}$	1599^{+104}_{-79}	$0.10^{+0.15}_{-0.09}$	$0.51^{+0.32}_{-0.38}$
Tortugal	1506 ± 24	1648^{+193}_{-91}	$0.15^{+0.29}_{-0.13}$	$0.50^{+0.31}_{-0.38}$	1813^{+157}_{-149}	$0.29^{+0.18}_{-0.24}$	$0.45^{+0.32}_{-0.27}$

[a]Crystallization temperature used in the inversion model.
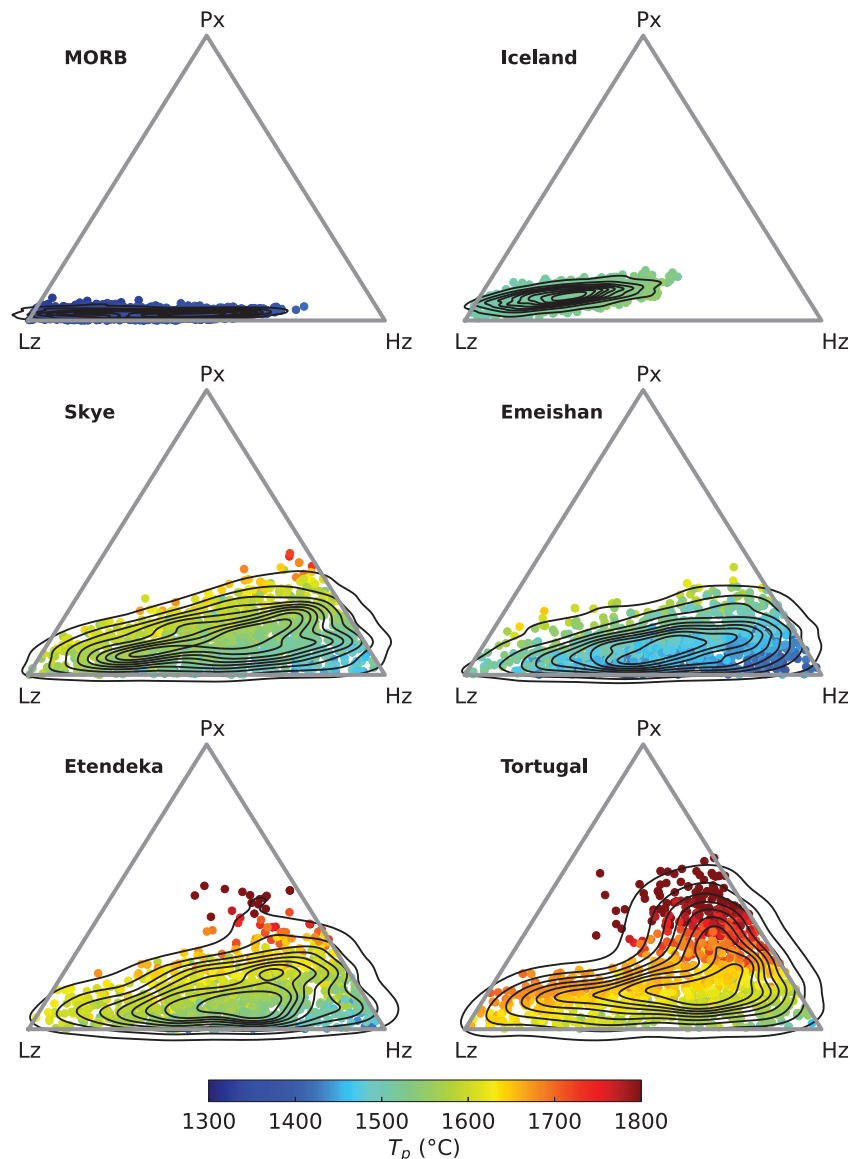
Fig. 12. Mantle lithologies and melting temperatures determined by our inversion analysis of natural samples using our extended OSAT, the contour lines represent density plot of the results.

calculated from inversion. For the modeling, we use the thermodynamic database of Holland *et al.* (2018). The KLB-1 peridotite (Wasylenki *et al.,* 2003) and MIX1G pyroxenite (Hirschmann *et al.,* 2003) were mixed with the median ratio of the estimated lithological fractions to generate an equilibrated melt with the mantle source for each locality. The equilibrated melt then crystallizes mineral phases within a given temperature interval at the base of the crust (same as the inversion model, see Table S3 in the supplementary data set and Table 1 in Matthews *et al.,* 2021) at each locality. The model results are compared to our estimated crystallization temperatures at each locality in Fig. 11. The equilibrated olivine usually includes sub-populations
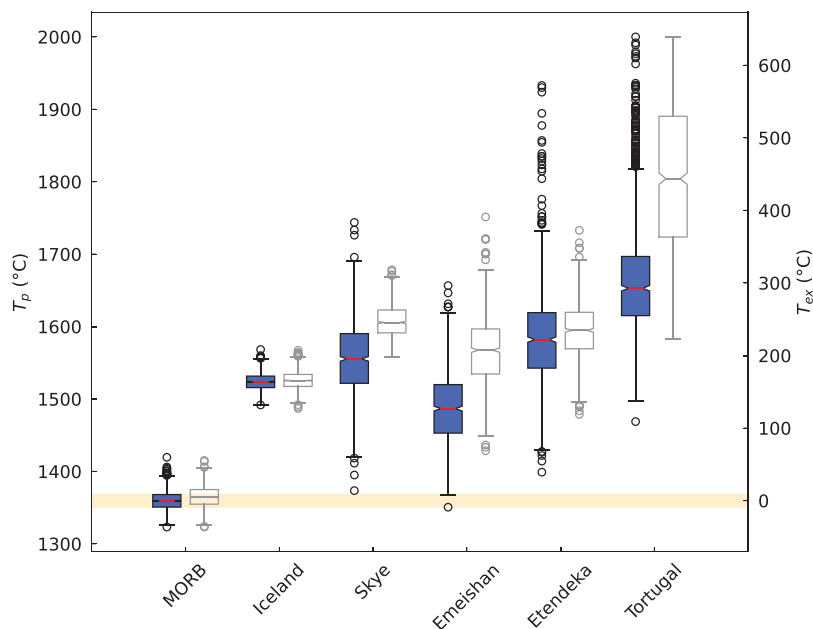
Fig. 13. Comparison of estimated mantle potential temperatures in this study (colored) with those of Matthews *et al.* (2021; gray). The temperature excess on the right axis is calculated here relative to the median T_p of MORB (Siqueiros). The heights of the boxes show the interquartile range (25th–75th), and the upper and lower whisker bars show maximum and minimum values beyond which, data points represent outliers.

containing higher-Fo ($>Fo_{91}$) than those in the erupted lavas, but are generally consistent with the crystallization temperatures calculated using our extended OSAT, whereas the results of Coogan *et al.* (2014) mostly overestimate the temperature.

CONCLUSIONS

We revised the formalism of the olivine-spinel aluminum exchange thermometer by performing new experiments and reanalyzing published experiments to extend the calibration P, T, fO_2, and H_2O conditions. Three models were regressed on the extended data set: a thermodynamic-based model (Eq. 5) and two empirical models (Eqs. 7 and 8). The thermodynamic model of Eq. 5 shows the best performance with the lowest uncertainties. The exchange of Al and Cr between olivine and spinel significantly effects the results when using the empirical models, whereas fO_2, water, and pressure have little to moderate effects on all models. The empirical models may only be accurate within a restricted spinel composition, leading to temperature overestimations by ~30–100°C in some intra-plate LIPs, but only minor differences in Iceland and MOR. These improved T_{cry} estimates translate to a significant difference in the mantle T_p and lithological fractions calculated for the investigated intra-plate LIPs.

ACKNOWLDEGEMENT

DATA AVAILABILITY

Additional data is available as supplementary electronic files. All calculations of each model, the protocol to choose the results are written in a python script and Excel spreadsheet (https://github.com/eazzzon/olspthermo).

SUPPLEMENTARY DATA

Supplementary data are available at Journal of Petrology online.

CONFLICT OF INTEREST

The authors declare no conflicts of interest.

References

Abouchami, W., Hofmann, A. W., Galer, S. J. G., Frey, F. A., Eisele, J. & Feigenson, M. (2005). Lead isotopes reveal bilateral asymmetry and vertical continuity in the Hawaiian mantle plume. *Nature* **434**, 851–856. https://doi.org/10.1038/nature03402.

Alvarado, G. E., Denyer, P. & Sinton, C. W. (1997). The 89 ma Tortugal komatiitic suite, Costa Rica: implications for a common geological origin of the Caribbean and eastern Pacific region from a mantle plume. *Geology* **25**, 439–442. https://doi.org/10.1130/0091-7613(1997)025<0439:TMTKSC>2.3.CO;2.

Ariskin, A. A. & Nikolaev, G. S. (1996). An empirical model for the calculation of spinel-melt equilibria in mafic igneous systems at atmospheric pressure: 1. Chromian spinels. *Contributions to Mineralogy and Petrology* **123**, 282–292. https://doi.org/10.1007/s004100050156.

Ballhaus, C., Berry, R. F. & Green, D. H. (1991). High pressure experimental calibration of the olivine-orthopyroxene-spinel oxygen geobarometer: implications for the oxidation state of the upper mantle. *Contributions to Mineralogy and Petrology*. **107**, 27–40. https://doi.org/10.1007/BF00311183.

Barr, J. A., Grove, T. L. & Wilson, A. H. (2009). Hydrous komatiites from Commondale, South Africa: an experimental study. *Earth*

and Planetary Science Letters **284**, 199–207. https://doi.org/10.1016/j.epsl.2009.04.029.

Batanova, V. G., Sobolev, A. V. & Kuzmin, D. V. (2015). Trace element analysis of olivine: high precision analytical method for JEOL JXA-8230 electron probe microanalyser. *Chemical Geology* **419**, 149–157. https://doi.org/10.1016/j.chemgeo.2015.10.042.

Batanova, V. G., Thompson, J. M., Danyushevsky, L. V., Portnyagin, M. V., Garbe-Schönberg, D., Hauri, E., Kimura, J. I., Chang, Q., Senda, R., Goemann, K., Chauvel, C., Campillo, S., Ionov, D. A. & Sobolev, A. V. (2019). New olivine reference material for in situ microanalysis. *Geostandards and Geoanalytical Research* **43**, 453–473. https://doi.org/10.1111/ggr.12266.

Beattie, P. (1993). Olivine-melt and orthopyroxene-melt equilibria. *Contributions to Mineralogy and Petrology.* **115**, 103–111. https://doi.org/10.1007/BF00712982.

Bechon, T., Billon, M., Namur, O., Bolle, O., Fugmann, P., Foucart, H., Devidal, J.-L., Delmelle, N. & Vander Auwera, J. (2022). Petrology of the magmatic system beneath Osorno volcano (central southern volcanic zone, Chile). *Lithos* **426-427**, 106777. https://doi.org/10.1016/j.lithos.2022.106777.

Blundy, J., Melekhova, E., Ziberna, L., Humphreys, M. C. S., Cerantola, V., Brooker, R. A., McCammon, C. A., Pichavant, M. & Ulmer, P. (2020). Effect of redox on Fe–mg–Mn exchange between olivine and melt and an oxybarometer for basalts. *Contributions to Mineralogy and Petrology* **175**, 103. https://doi.org/10.1007/s00410-020-01736-7.

Borisova, A. Y., Zagrtdenov, N. R., Toplis, M. J. & Guignard, J. (2020). New model of chromite and magnesiochromite solubility in silicate melts. arXiv preprint.

Brown Krein, S., Molitor, Z. J. & Grove, T. L. (2021). ReversePetrogen: a multiphase dry reverse fractional crystallization-mantle melting Thermobarometer applied to 13,589 Mid-Ocean ridge basalt glasses. *Journal of Geophysical Research: Solid Earth* **126**, e2020JB021292. https://doi.org/10.1029/2020JB021292.

Buchner, J., Georgakakis, A., Nandra, K., Hsu, L., Rangel, C., Brightman, M., Merloni, A., Salvato, M., Donley, J. & Kocevski, D. (2014). X-ray spectral modelling of the AGN obscuring region in the CDFS: Bayesian model selection and catalogue. *Astronomy & Astrophysics* **564**, A125. https://doi.org/10.1051/0004-6361/201322971.

Campbell, I. H. & Griffiths, R. W. (1990). Implications of mantle plume structure for the evolution of flood basalts. *Earth and Planetary Science Letters* **99**, 79–93. https://doi.org/10.1016/0012-821X(90)90072-6.

Charlier, B., Grove, T. L., Namur, O. & Holtz, F. (2018). Crystallization of the lunar magma ocean and the primordial mantle-crust differentiation of the moon. *Geochimica et Cosmochimica Acta* **234**, 50–69. https://doi.org/10.1016/j.gca.2018.05.006.

Chung, S.-L. & Jahn, B. (1995). Plume-lithosphere interaction in generation of the Emeishan flood basalts at the Permian-Triassic boundary. *Geology* **23**, 889–892. https://doi.org/10.1130/0091-7613(1995)023<0889:PLIIGO>2.3.CO;2.

Coogan, L. A., Saunders, A. D. & Wilson, R. N. (2014). Aluminum-in-olivine thermometry of primitive basalts: evidence of an anomalously hot mantle source for large igneous provinces. *Chemical Geology* **368**, 1–10. https://doi.org/10.1016/j.chemgeo.2014.01.004.

D'Souza, R. J., Canil, D. & Coogan, L. A. (2020). Geobarometry for spinel peridotites using Ca and Al in olivine. *Contributions to Mineralogy and Petrology* **175**, 5. https://doi.org/10.1007/s00410-019-1647-6.

Darken, L. S. & Gurry, R. W. (1953) *Physical chemistry of metals*. New York: McGraw-Hill.

Droop, G. T. R. (1987). A general equation for estimating Fe^{3+} concentrations in ferromagnesian silicates and oxides from microprobe analyses, using stoichiometric criteria. *Mineralogical Magazine* **51**, 431–435. https://doi.org/10.1180/minmag.1987.051.361.10.

Evans, T. M., O'Neill, C. H. S. & Tuff, J. (2008). The influence of melt composition on the partitioning of REEs, Y, Sc, Zr and Al between forsterite and melt in the system CMAS. *Geochimica et Cosmochimica Acta* **72**, 5708–5721. https://doi.org/10.1016/j.gca.2008.09.017.

Falloon, T. J., Danyushevsky, L. V., Ariskin, A., Green, D. H. & Ford, C. E. (2007). The application of olivine geothermometry to infer crystallization temperatures of parental liquids: implications for the temperature of MORB magmas. *Chemical Geology* **241**, 207–233. https://doi.org/10.1016/j.chemgeo.2007.01.015.

Feroz, F. & Hobson, M. P. (2008). Multimodal nested sampling: an efficient and robust alternative to Markov chain Monte Carlo methods for astronomical data analyses. *Monthly Notices of the Royal Astronomical Society* **384**, 449–463. https://doi.org/10.1111/j.1365-2966.2007.12353.x.

Feroz, F., Hobson, M. P. & Bridges, M. (2009). MultiNest: an efficient and robust Bayesian inference tool for cosmology and particle physics. *Monthly Notices of the Royal Astronomical Society* **398**, 1601–1614. https://doi.org/10.1111/j.1365-2966.2009.14548.x.

Feroz, F., Hobson, M. P., Cameron, E. & Pettitt, A. N. (2013). Importance nested sampling and the MultiNest algorithm. arXiv preprint arXiv:1306.2144.

Ganguly, J. (2008) *Thermodynamics in earth and planetary sciences*. Berlin: Springer.

Gavrilenko, M., Batanova, V. G., Llovet, X., Krasheninnikov, S., Koshlyakova, A. N. & Sobolev, A. V. (2023). Secondary fluorescence effect quantification of EPMA analyses of olivine grains embedded in basaltic glass. *Chemical Geology.* **621**, 121328. https://doi.org/10.1016/j.chemgeo.2023.121328.

Gavrilenko, M., Ozerov, A., Kyle, P. R., Carr, M. J., Nikulin, A., Vidito, C. & Danyushevsky, L. (2023). Abrupt transition from fractional crystallization to magma mixing at Gorely volcano (Kamchatka) after caldera collapse. *Bulletin of Volcanology.* **78**, 47.

Gee, L. L. & Sack, R. O. (1988). Experimental petrology of Melilite Nephelinites. *Journal of Petrology* **29**, 1233–1255. https://doi.org/10.1093/petrology/29.6.1233.

van Gerve, T., Namur, O., Wieser, P., Lamadrid, H., Hulsbosch, N. & Neave, D. (2021). Constraints on deep magmatic volatile budgets from olivine hosted melt inclusions: integrating 3D imaging with chemical microanalysis. *AGU Fall Meeting Abstracts*, V41C–V03C.

Ghiorso, M. S. (1990). Application of the Darken equation to mineral solid solutions with variable degrees of order-disorder. *American Mineralogist* **75**, 539–543.

Ghiorso, M. S. & Sack, R. O. (1995). Chemical mass transfer in magmatic processes IV. A revised and internally consistent thermodynamic model for the interpolation and extrapolation of liquid-solid equilibria in magmatic systems at elevated temperatures and pressures. *Contributions to Mineralogy and Petrology* **119**, 197–212. https://doi.org/10.1007/BF00307281.

Ghiorso, M. S., Hirschmann, M. M., Reiners, P. W. & Kress, V. C. (2002). The pMELTS: a revision of MELTS for improved calculation of phase relations and major element partitioning related to partial melting of the mantle to 3 GPa. *Geochemistry, Geophysics, Geosystems* **3**, 1–35. https://doi.org/10.1029/2001GC000217.

Gibson, S. A. (2002). Major element heterogeneity in Archean to recent mantle plume starting-heads. *Earth and Planetary Science Letters* **195**, 59–74. https://doi.org/10.1016/S0012-821X(01)00566-0.

Goltz, A. E., Krawczynski, M. J., Gavrilenko, M., Gorbach, N. V. & Ruprecht, P. (2020). Evidence for superhydrous primitive arc magmas from mafic enclaves at Shiveluch volcano. *Kamchatka.*

Contributions to Mineralogy and Petrology. **175**, 1–26. https://doi.org/10.1007/s00410-020-01746-5.

Green, D. H. & Falloon, T. J. (2005) Primary magmas at mid-ocean ridges,"hotspots," and other intraplate settings: Constraints on mantle potential temperature. In: Foulger G. R., Natland J. H., Presnall D. C. & Anderson D. L. (eds) *Plates, plumes and paradigms*. Geological Society of America, pp.217–247.

Gregg, P. M., Behn, M. D., Lin, J. & Grove, T. L. (2009). Melt generation, crystallization, and extraction beneath segmented oceanic transform faults. *Journal of Geophysical Research: Solid Earth* **114**. https://doi.org/10.1029/2008JB006100.

Grove, T. L., Kinzler, R. J. & Bryan, W. B. (2013). Fractionation of mid-ocean ridge basalt (MORB). *Mantle flow and melt generation at mid-ocean ridges.* **71**, 281–310. https://doi.org/10.1029/GM071p0281.

Guo, S., Ye, K., Chen, Y. & Liu, J.-B. (2009). A normalization solution to mass transfer illustration of multiple progressively altered samples using the isocon diagram. *Economic Geology* **104**, 881–886. https://doi.org/10.2113/gsecongeo.104.6.881.

Hamecher, E. A., Antoshechkina, P. M., Ghiorso, M. S. & Asimow, P. D. (2013). The molar volume of FeO–MgO–Fe2O3–Cr2O3–Al2O3–TiO2 spinels. *Contributions to Mineralogy and Petrology* **165**, 25–43.

Hanson, B. & Jones, J. H. (1998). The systematics of Cr3+ and Cr2+ partitioning between olivine and liquid in the presence of spinel. *American Mineralogist* **83**, 669–684. https://doi.org/10.2138/am-1998-7-801.

Heinonen, J. S., Jennings, E. S. & Riley, T. R. (2015). Crystallisation temperatures of the most mg-rich magmas of the Karoo LIP on the basis of Al-in-olivine thermometry. *Chemical Geology* **411**, 26–35. https://doi.org/10.1016/j.chemgeo.2015.06.015.

Herzberg, C. & Asimow, P. D. (2015). PRIMELT3 MEGA.XLSM software for primary magma calculation: Peridotite primary magma MgO contents from the liquidus to the solidus. *Geochemistry, Geophysics, Geosystems* **16**, 563–578. https://doi.org/10.1002/2014GC005631.

Herzberg, C., Asimow, P. D., Arndt, N., Niu, Y., Lesher, C. M., Fitton, J. G., Cheadle, M. J. & Saunders, A. D. (2007). Temperatures in ambient mantle and plumes: constraints from basalts, picrites, and komatiites. *Geochemistry, Geophysics, Geosystems* **8**. https://doi.org/10.1029/2006GC001390.

Hirschmann, M. M., Kogiso, T., Baker, M. B. & Stolper, E. M. (2003). Alkalic magmas generated by partial melting of garnet pyroxenite. *Geology* **31**, 481–484. https://doi.org/10.1130/0091-7613(2003)031<0481:AMGBPM>2.0.CO;2.

Holland, T. J., Green, E. C. & Powell, R. (2018). Melting of peridotites through to granites: a simple thermodynamic model in the system KNCFMASHTOCr. *Journal of Petrology* **59**, 881–900. https://doi.org/10.1093/petrology/egy048.

Hu, W.-J., Zhou, M.-F., Yudovskaya, M. A., Vikentyev, I. V., Malpas, J. & Zhang, P.-F. (2022). Trace elements in chromite as indicators of the origin of the Giant Podiform chromite deposit at Kempirsai, Kazakhstan. *Economic Geology* **117**, 1629–1655. https://doi.org/10.5382/econgeo.4955.

Ito, M. & Ganguly, J. (2006). Diffusion kinetics of Cr in olivine and 53Mn–53Cr thermochronology of early solar system objects. *Geochimica et Cosmochimica Acta* **70**, 799–809. https://doi.org/10.1016/j.gca.2005.09.020.

Jennings, E. S., Gibson, S. A. & Maclennan, J. (2019). Hot primary melts and mantle source for the Paraná-Etendeka flood basalt province: new constraints from Al-in-olivine thermometry. *Chemical Geology* **529**, 119287. https://doi.org/10.1016/j.chemgeo.2019.119287.

Jennings, E., Buisman, I. & Coull, P. (2020). Investigating mantle melting temperatures on earth, Mars and the moon using Al-in-olivine thermometry. *AGU Fall Meeting Abstracts* .

Jochum, K. P., Stoll, B., Herwig, K., Willbold, M., Hofmann, A. W., Amini, M., Aarburg, S., Abouchami, W., Hellebrand, E., Mocek, B., Raczek, I., Stracke, A., Alard, O., Bouman, C., Becker, S., Dücking, M., Brätz, H., Klemd, R., de Bruin, D., Canil, D., Cornell, D., de Hoog, C. J., Dalpé, C., Danyushevsky, L., Eisenhauer, A., Gao, Y., Snow, J. E., Groschopf, N., Günther, D., Latkoczy, C., Guillong, M., Hauri, E. H., Höfer, H. E., Lahaye, Y., Horz, K., Jacob, D. E., Kasemann, S. A., Kent, A. J. R., Ludwig, T., Zack, T., Mason, P. R. D., Meixner, A., Rosner, M., Misawa, K., Nash, B. P., Pfänder, J., Premo, W. R., Sun, W. D., Tiepolo, M., Vannucci, R., Vennemann, T., Wayne, D. & Woodhead, J. D. (2006). MPI-DING reference glasses for in situ microanalysis: new reference values for element concentrations and isotope ratios. *Geochemistry, Geophysics, Geosystems* **7**. https://doi.org/10.1029/2005GC001060.

Jollands, M. C., O'Neill, H. S. C., Van Orman, J., Berry, A. J., Hermann, J., Newville, M. & Lanzirotti, A. (2018). Substitution and diffusion of Cr2+ and Cr3+ in synthetic forsterite and natural olivine at 1200–1500 °C and 1 bar. *Geochimica et Cosmochimica Acta* **220**, 407–428. https://doi.org/10.1016/j.gca.2017.09.030.

Kamenetsky, V. S., Crawford, A. J. & Meffre, S. (2001). Factors controlling chemistry of magmatic spinel: an empirical study of associated olivine, Cr-spinel and melt inclusions from primitive rocks. *Journal of Petrology* **42**, 655–671. https://doi.org/10.1093/petrology/42.4.655.

Katsura, T. & Ito, E. (1989). The system Mg2SiO4-Fe2SiO4 at high pressures and temperatures: precise determination of stabilities of olivine, modified spinel, and spinel. *Journal of Geophysical Research: Solid Earth* **94**, 15663–15670. https://doi.org/10.1029/JB094iB11p15663.

Koshlyakova, A. N., Sobolev, A. V., Krasheninnikov, S. P., Batanova, V. G. & Borisov, A. A. (2022). Ni partitioning between olivine and highly alkaline melts: an experimental study. *Chemical Geology* **587**, 120615. https://doi.org/10.1016/j.chemgeo.2021.120615.

Krasheninnikov, S. P., Sobolev, A. V., Batanova, V. G., Kargaltsev, A. A. & Borisov, A. A. (2017). Experimental testing of olivine–melt equilibrium models at high temperatures. *Doklady Earth Sciences* **475**, 919–922. https://doi.org/10.1134/S1028334X17080153.

Lang, S., Mollo, S., France, L., Misiti, V. & Nazzari, M. (2022). Partitioning of Ti, Al, P, and Cr between olivine and a tholeiitic basaltic melt: insights on olivine zoning patterns and cation substitution reactions under variable cooling rate conditions. *Chemical Geology* **601**, 120870. https://doi.org/10.1016/j.chemgeo.2022.120870.

Li, J., Huang, X.-L., Li, X.-H., Chu, F.-Y., Zhu, J.-H., Zhu, Z.-M. & Wang, H. (2021). Anomalously hot mantle source beneath the dragon flag Supersegment of the southwest Indian ridge: new evidence from crystallisation temperatures of mid-ocean ridge basalts. *Lithos* **396-397**, 106221. https://doi.org/10.1016/j.lithos.2021.106221.

Llovet, X. & Salvat, F. (2017). PENEPMA: a Monte Carlo program for the simulation of X-ray emission in electron probe microanalysis. *Microscopy and Microanalysis* **23**, 634–646. https://doi.org/10.1017/S1431927617000526.

Llovet, X., Pinard, P. T., Donovan, J. J. & Salvat, F. (2012). Secondary fluorescence in electron probe microanalysis of material couples. *Journal of Physics D: Applied Physics* **45**, 225301. https://doi.org/10.1088/0022-3727/45/22/225301.

Llovet, X., Gavrilenko, M., Batanova, V. G. & Sobolev, A. V. (2023). Element depletion due to missing boundary fluorescence in electron probe microanalysis: the case of Ni in olivine. *Microscopy and Microanalysis* **29**, 1595–1609. https://doi.org/10.1093/micmic/ozad100.

Matthews, S., Shorttle, O. & Maclennan, J. (2016). The temperature of the Icelandic mantle from olivine-spinel aluminum exchange thermometry: mantle temperature from geothermometry.

Geochemistry, Geophysics, Geosystems **17**, 4725–4752. https://doi.org/10.1002/2016GC006497.

Matthews, S., Wong, K., Shorttle, O., Edmonds, M. & Maclennan, J. (2021). Do olivine crystallization temperatures faithfully record mantle temperature variability? *Geochemistry, Geophysics, Geosystems* **22**, e2020GC009157. https://doi.org/10.1029/2020GC009157.

Matthews, S., Wong, K. & Gleeson, M. (2022). PyMelt: an extensible python engine for mantle melting calculations. *Volcanica* **5**(2), 469–475. https://doi.org/10.30909/vol.05.02.469475.

Matzen, A. K., Baker, M. B., Beckett, J. R. & Stolper, E. M. (2011). Fe–mg partitioning between olivine and high-magnesian melts and the nature of Hawaiian parental liquids. *Journal of Petrology* **52**, 1243–1263. https://doi.org/10.1093/petrology/egq089.

Matzen, A. K., Baker, M. B., Beckett, J. R. & Stolper, E. M. (2013). The temperature and pressure dependence of nickel partitioning between olivine and silicate melt. *Journal of Petrology* **54**, 2521–2545. https://doi.org/10.1093/petrology/egt055.

Mckenzie, D. A. N. & Bickle, M. J. (1988). The volume and composition of melt generated by extension of the lithosphere. *Journal of Petrology* **29**, 625–679. https://doi.org/10.1093/petrology/29.3.625.

Médard, E. & Grove, T. L. (2008). The effect of H_2O on the olivine liquidus of basaltic melts: experiments and thermodynamic models. *Contributions to Mineralogy and Petrology* **155**, 417–432. https://doi.org/10.1007/s00410-007-0250-4.

Milman-Barris, M. S., Beckett, J. R., Baker, M. B., Hofmann, A. E., Morgan, Z., Crowley, M. R., Vielzeuf, D. & Stolper, E. (2008). Zoning of phosphorus in igneous olivine. *Contributions to Mineralogy and Petrology* **155**, 739–765. https://doi.org/10.1007/s00410-007-0268-7.

Mitchell, A. L. & Grove, T. L. (2015). Melting the hydrous, subarc mantle: the origin of primitive andesites. *Contributions to Mineralogy and Petrology* **170**, 13. https://doi.org/10.1007/s00410-015-1161-4.

Molendijk, S. M., Namur, O., Kaeghetso, E. K., Mason, P. R. D., Smets, B., Vander Auwera, J. E. & Neave, D. A. (2023a, 2023). Petrology of the Nyiragongo volcano, DR Congo Goldschmidt.

Molendijk, S. M., Namur, O., Mason, P. R., Dubacq, B., Smets, B., Neave, D. A. & Charlier, B. (2023b). Trace element partitioning in silica-undersaturated alkaline magmatic systems. *Geochimica et Cosmochimica Acta* **346**, 29–53. https://doi.org/10.1016/j.gca.2023.01.025.

Morgan, W. J. (1971). Convection plumes in the lower mantle. *Nature* **230**, 42–43. https://doi.org/10.1038/230042a0.

Neave, D. A. & Namur, O. (2022). Plagioclase archives of depleted melts in the oceanic crust. *Geology* **50**, 848–852. https://doi.org/10.1130/G49840.1.

Neave, D. A., Namur, O., Shorttle, O. & Holtz, F. (2019). Magmatic evolution biases basaltic records of mantle chemistry towards melts from recycled sources. *Earth and Planetary Science Letters* **520**, 199–211. https://doi.org/10.1016/j.epsl.2019.06.003.

O'Hara, M. (1968). Are ocean floor basalts primary magma? *Nature* **220**, 683–686. https://doi.org/10.1038/220683a0.

Parman, S. W. & Grove, T. L. (2004). Harzburgite melting with and without H_2O: experimental data and predictive modeling: Harzburgite melting. *Journal of Geophysical Research: Solid Earth* **109**. https://doi.org/10.1029/2003JB002566.

Phipps Morgan, J. (2001). Thermodynamics of pressure release melting of a veined plum pudding mantle. *Geochemistry, Geophysics, Geosystems* **2**. https://doi.org/10.1029/2000GC000049.

Poustovetov, A. & Roeder, P. (2001). Numerical modeling of major element distribution between chromian spinel and basaltic melt, with application to chromian spinel in MORBs. *Contributions to Mineralogy and Petrology* **142**, 58–71. https://doi.org/10.1007/s004100100272.

Prissel, T. C., Gross, J. & Draper, D. S. (2017) Application of Olivine-Spinel Eqilibria to Extraterrestrial Igneous Systems. In: *Lunar and Planetary Sciences Conference*. No. JSC-CN-38578.

Putirka, K. D. (2005). Mantle potential temperatures at Hawaii, Iceland, and the mid-ocean ridge system, as inferred from olivine phenocrysts: evidence for thermally driven mantle plumes. *Geochemistry, Geophysics, Geosystems* **6**. https://doi.org/10.1029/2005GC000915.

Putirka, K. D. (2008). Thermometers and barometers for volcanic systems. *Reviews in Mineralogy and Geochemistry* **69**, 61–120. https://doi.org/10.2138/rmg.2008.69.3.

Putirka, K. (2016). Rates and styles of planetary cooling on earth, moon, Mars, and Vesta, using new models for oxygen fugacity, ferric-ferrous ratios, olivine-liquid Fe–Mg exchange, and mantle potential temperature. *American Mineralogist* **101**, 819–840. https://doi.org/10.2138/am-2016-5402.

Putirka, K. D., Perfit, M., Ryerson, F. J. & Jackson, M. G. (2007). Ambient and excess mantle temperatures, olivine thermometry, and active vs. passive upwelling. *Chemical Geology* **241**, 177–206. https://doi.org/10.1016/j.chemgeo.2007.01.014.

Ramsey, S. R., Howarth, G. H., Udry, A. & Gross, J. (2021). Nickel–manganese variability in olivine and Al-in-olivine thermometry for olivine-phyric shergottites. *Meteoritics & Planetary Science* **56**(8), 1597–1618. https://doi.org/10.1111/maps.13721.

Riel, N., Kaus, B. J. P., Green, E. C. R. & Berlie, N. (2022). MAGEMin, an efficient Gibbs energy minimizer: application to igneous systems. *Geochemistry, Geophysics, Geosystems* **23**, e2022GC010427. https://doi.org/10.1029/2022GC010427.

Roeder, P. L. & Emslie, R. F. (1970). Olivine-liquid equilibrium. *Contributions to Mineralogy and Petrology* **29**, 275–289. https://doi.org/10.1007/BF00371276.

Sack, R. O. (1982). Spinels as petrogenetic indicators: activity-composition relations at low pressures. *Contributions to Mineralogy and Petrology* **79**, 169–186. https://doi.org/10.1007/BF01132886.

Sack, R. O. & Ghiorso, M. S. (1991a). An internally consistent model for the thermodynamic properties of Fe−mg-titanomagnetite-aluminate spinels. *Contributions to Mineralogy and Petrology* **106**, 474–505. https://doi.org/10.1007/BF00321989.

Sack, R. O. & Ghiorso, M. S. (1991b). Chromian spinels as petrogenetic indicators: thermodynamics and petrological applications. *American Mineralogist* **76**, 827–847.

Shea, T., Hammer, J. E., Hellebrand, E., Mourey, A. J., Costa, F., First, E. C., Lynn, K. J. & Melnik, O. (2019). Phosphorus and aluminum zoning in olivine: contrasting behavior of two nominally incompatible trace elements. *Contributions to Mineralogy and Petrology* **174**, 85. https://doi.org/10.1007/s00410-019-1618-y.

Shorttle, O., Maclennan, J. & Lambart, S. (2014). Quantifying lithological variability in the mantle. *Earth and Planetary Science Letters* **395**, 24–40. https://doi.org/10.1016/j.epsl.2014.03.040.

Sleep, N. H. (1992). Time dependence of mantle plumes: some simple theory. *Journal of Geophysical Research: Solid Earth* **97**, 20007–20019. https://doi.org/10.1029/92JB01468.

Sleep, N. H. (1996). Lateral flow of hot plume material ponded at sublithospheric depths. *Journal of Geophysical Research: Solid Earth* **101**, 28065–28083. https://doi.org/10.1029/96JB02463.

Snedecor, G. W. & Cochran, W. G. (1989) Statistical methods. In: *Ames*, 8thEdn edn. Ames, Iowa: Iowa state University Press, 54, pp.71–82.

Sobolev, A. V., Asafov, E. V., Gurenko, A. A., Arndt, N. T., Batanova, V. G., Portnyagin, M. V., Garbe-Schönberg, D. & Krasheninnikov, S. P. (2016). Komatiites reveal a hydrous Archaean deep-mantle reservoir. *Nature* **531**, 628–632. https://doi.org/10.1038/nature17152.

Sossi, P. A., Klemme, S., O'Neill, H. S. & C., Berndt, J. & Moynier, F. (2019). Evaporation of moderately volatile elements from silicate

melts: experiments and theory. *Geochimica et Cosmochimica Acta* **260**, 204–231. https://doi.org/10.1016/j.gca.2019.06.021.

Spandler, C. & O'Neill, H. S. C. (2010). Diffusion and partition coefficients of minor and trace elements in San Carlos olivine at 1,300°C with some geochemical implications. *Contributions to Mineralogy and Petrology* **159**, 791–818. https://doi.org/10.1007/s00410-009-0456-8.

Spice, H. E., Fitton, J. G. & Kirstein, L. A. (2016). Temperature fluctuation of the Iceland mantle plume through time: Iceland mantle plume *t* fluctuations. *Geochemistry, Geophysics, Geosystems* **17**, 243–254. https://doi.org/10.1002/2015GC006059.

Stroncik, N. A., Trumbull, R. B., Krienitz, M.-S., Niedermann, S., Romer, R. L., Harris, C. & Day, J. (2017). Helium isotope evidence for a deep-seated mantle plume involved in South Atlantic breakup. *Geology* **45**, 827–830. https://doi.org/10.1130/G39151.1.

Thompson, J. B., Jr. (1969). Chemical reactions in crystals. *American Mineralogist: Journal of Earth and Planetary Materials* **54**, 341–375.

Thompson, R. N., Gibson, S. A., Dickin, A. P. & Smith, P. M. (2001). Early cretaceous basalt and picrite dykes of the southern Etendeka region, NW Namibia: windows into the role of the Tristan mantle plume in Paraná–Etendeka magmatism. *Journal of Petrology* **42**, 2049–2081. https://doi.org/10.1093/petrology/42.11.2049.

Thy, P. (1995). Low-pressure experimental constraints on the evolution of komatiites. *Journal of Petrology* **36**, 1529–1548.

Toplis, M. J. (2005). The thermodynamics of iron and magnesium partitioning between olivine and liquid: criteria for assessing and predicting equilibrium in natural and experimental systems. *Contributions to Mineralogy and Petrology* **149**, 22–39. https://doi.org/10.1007/s00410-004-0629-4.

Toplis, M. J. & Carroll, M. R. (1995). An experimental study of the influence of oxygen fugacity on Fe-Ti oxide stability, phase relations, and mineral–melt Equilibria in Ferro-basaltic systems. *Journal of Petrology* **36**, 1137–1170. https://doi.org/10.1093/petrology/36.5.1137.

Trela, J., Gazel, E., Sobolev, A. V., Moore, L., Bizimis, M., Jicha, B. & Batanova, V. G. (2017). The hottest lavas of the Phanerozoic and the survival of deep Archaean reservoirs. *Nature Geoscience* **10**, 451–456. https://doi.org/10.1038/ngeo2954.

Tuff, J., Takahashi, E. & Gibson, S. A. (2005). Experimental constraints on the role of garnet Pyroxenite in the genesis of high-Fe mantle plume derived melts. *Journal of Petrology* **46**, 2023–2058. https://doi.org/10.1093/petrology/egi046.

Vogt, K., Dohmen, R. & Chakraborty, S. (2015). Fe–Mg diffusion in spinel: new experimental data and a point defect model. *American Mineralogist* **100**, 2112–2122. https://doi.org/10.2138/am-2015-5109.

Wan, Z., Coogan, L. A. & Canil, D. (2008). Experimental calibration of aluminum partitioning between olivine and spinel as a geothermometer. *American Mineralogist* **93**, 1142–1147. https://doi.org/10.2138/am.2008.2758.

Wasylenki, L. E., Baker, M. B., Kent, A. J. & Stolper, E. M. (2003). Near-solidus melting of the shallow upper mantle: partial melting experiments on depleted peridotite. *Journal of Petrology* **44**, 1163–1191. https://doi.org/10.1093/petrology/44.7.1163.

White, R. & McKenzie, D. (1989). Magmatism at rift zones: the generation of volcanic continental margins and flood basalts. *Journal of Geophysical Research: Solid Earth* **94**, 7685–7729. https://doi.org/10.1029/JB094iB06p07685.

White, R. S. & McKenzie, D. (1995). Mantle plumes and flood basalts. *Journal of Geophysical Research: Solid Earth* **100**, 17543–17585. https://doi.org/10.1029/95JB01585.

Wu, Y.-D, Yan, J.-H., Stagno, V., Nekrylov, N., Wang, J.-T. & Wang, H. (2022). Redox heterogeneity of picritic lavas with respect to

their mantle sources in the Emeishan large igneous province. *Geochimica et Cosmochimica Acta*S0016703722000102 **320**, 161–178. https://doi.org/10.1016/j.gca.2022.01.001.

Xiao, L., Xu, Y. G., Mei, H. J., Zheng, Y. F., He, B. & Pirajno, F. (2004). Distinct mantle sources of low-Ti and high-Ti basalts from the western Emeishan large igneous province, SW China: implications for plume–lithosphere interaction. *Earth and Planetary Science Letters* **228**, 525–546. https://doi.org/10.1016/j.epsl.2004.10.002.

Xu, Q.-S. & Liang, Y.-Z. (2001). Monte Carlo cross validation. *Chemometrics and Intelligent Laboratory Systems* **56**, 1–11. https://doi.org/10.1016/S0169-7439(00)00122-2.

Xu, R. & Liu, Y. (2016). Al-in-olivine thermometry evidence for the mantle plume origin of the Emeishan large igneous province. *Lithos* **266-267**, 362–366. https://doi.org/10.1016/j.lithos.2016.10.016.

Xu, Y., Chung, S.-L., Jahn, B. & Wu, G. (2001). Petrologic and geochemical constraints on the petrogenesis of Permian–Triassic Emeishan flood basalts in southwestern China. *Lithos* **58**, 145–168. https://doi.org/10.1016/S0024-4937(01)00055-X.

Zhang, L., Ren, Z.-Y., Zhang, L., Wu, Y.-D, Qian, S.-P., Xia, X.-P. & Xu, Y.-G. (2021). Nature of the mantle plume under the Emeishan large Igneous Province: constraints from olivine-hosted melt inclusions of the Lijiang Picrites. *Journal of Geophysical Research: Solid Earth* **126**, e2020JB021022. https://doi.org/10.1029/2020JB021022.

Zhang, Y., Namur, O. & Charlier, B. (2023). Experimental study of high-Ti and low-Ti basalts: liquid lines of descent and silicate liquid immiscibility in large igneous provinces. *Contributions to Mineralogy and Petrology* **178**, 7. https://doi.org/10.1007/s00410-022-01990-x.

APPENDIX A. THERMODYNAMIC MODEL OF OLIVINE–SPINEL AL PARTITIONING

Here, we develop our thermodynamic formalism to understand the Al exchange between olivine and spinel. The most plausible solution mechanism for the incorporation of Al into olivine and Cr-spinel is (Coogan *et al.*, 2014):

$$\left(MgAl^{TET}\right)Al^{OCT}O_4^{Spl} = \left(MgAl^{TET}\right)Al^{OCT}O_4^{Ol} \tag{A.1}$$
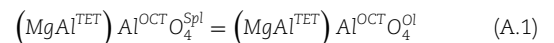
Thus, the equilibrium of the reaction is written as:

$$\mu_{\text{MgAl}_2\text{O}_4}^{\text{Ol}} = \mu_{\text{MgAl}_2\text{O}_4}^{\text{Spl}} \tag{A.2}$$

where μ_{a^b} is the chemical potential of component a in phase b. For a given phase:

$$\mu_a = \mu_a^0 + RT\ln\alpha^a \tag{A.3}$$

where μ_a^0 is the chemical potential of component a at standard state, α^a is the activity of component a, R is the universal gas constant [8.314 J mol^{-1} K^{-1}], and T is the absolute temperature in Kelvin.

For olivine, we can write:

$$\alpha_{\text{MgAl}_2\text{O}_4}^{\text{Ol}} = \gamma \times X_{\text{MgAl}_2\text{O}_4}^{\text{Ol}} \tag{A.4}$$

$$X_{\text{MgAl}_2\text{O}_4}^{\text{Ol}} = \left(Al_2O_3{}_{\text{wt\%}}^{\text{Ol}}/M_{\text{Al}_2\text{O}_3}\right) \times M_{\text{MgAl}_2\text{O}_4} \tag{A.5}$$

where γ is the activity coefficient and M the molar weight of the component, and X is the mole fraction. Combining Eqs. A.3–A.5, we obtain:

$$\mu_{\text{MgAl}_2\text{O}_4} = \mu_{\text{MgAl}_2\text{O}_4}^0 + RT\ln\left[\gamma \times \left(Al_2O_3{}_{\text{wt.\%}}^{\text{Ol}}/M_{\text{Al}_2\text{O}_3}\right) \times M_{\text{MgAl}_2\text{O}_4}\right] \tag{A.6}$$

Table A1: Independent compositional, ordering variables and definitions of site mole fractions

$X_2 = X_{Mg^{2+}}^{TET} + 2X_{Mg^{2+}}^{OCT}$	$X_{Mg^{2+}}^{TET} = \frac{X_2 + s_1}{2}$
$X_3 = X_{Cr^{3+}}^{TET} + X_{Cr^{3+}}^{OCT}$	$X_{Fe^{2+}}^{TET} = X_4 + s_2 + s_3 + s_4 - \frac{X_2 + s_1}{2}$
$X_4 = 2X_{Ti^{4+}}^{OCT}$	$X_{Fe^{3+}}^{TET} = X_5 - s_4$
$X_5 = X_{Fe^{3+}}^{TET} + 2X_{Fe^{3+}}^{OCT}$	$X_{Al^{3+}}^{TET} = 1 - X_3 - X_4 - X_5 - s_2$
$s_1 = X_{Mg^{2+}}^{TET} - 2X_{Mg^{2+}}^{OCT}$	$X_{Cr^{3+}}^{TET} = X_3 - s_3$
$s_2 = \frac{2X_{Al^{3+}}^{OCT} - X_{Al^{3+}}^{TET}}{2}$	$X_{Mg^{2+}}^{OCT} = \frac{X_2 - s_1}{4}$
$s_3 = \frac{2X_{Cr^{3+}}^{OCT} - X_{Cr^{3+}}^{TET}}{2}$	$X_{Fe^{2+}}^{OCT} = \frac{1 - s_2 - s_3 - s_4}{2} - \frac{X_2 - s_1}{4}$
$s_4 = \frac{2X_{Fe^{3+}}^{OCT} - X_{Fe^{3+}}^{TET}}{2}$	$X_{Fe^{3+}}^{OCT} = \frac{X_5 + s_4}{2}$
$X_{Fe^{2+}}^{TET} + X_{Fe^{2+}}^{TET} + X_{Al^{3+}}^{TET} + X_{Cr^{3+}}^{TET} + X_{Fe^{3+}}^{TET} = 1$	$X_{Al^{3+}}^{OCT} = \frac{1 - X_3 - X_4 - X_5 + s_2}{2}$
$X_{Fe^{2+}}^{OCT} + X_{Mg^2}^{OCT} + X_{Al^{3+}}^{OCT} + X_{Cr^{3+}}^{OCT} + X_{Fe^{3+}}^{OCT} + X_{Ti^{4+}}^{OCT} = 1$	$X_{Cr^{3+}}^{OCT} = \frac{X_3 + s_3}{2}$
	$X_{Ti^{4+}}^{OCT} = \frac{X_4}{2}$

We apply a thermodynamic model involving cation site ordering (Sack, 1982; Sack & Ghiorso, 1991a, 1991b) to describe the thermodynamic properties of the components in Cr-spinel. In this model, spinel is assumed to be stoichiometrically perfect (R_3O_4), with *Fd3m* space group symmetry. Five 'fictive' independent compositional variables (X_i) and ordering parameters (s_i) are needed to describe the compositional change in Cr-spinel, which can be calculated from mole fractions of cations in the spinel.

The independent compositional and ordering variables as well as the definitions of site mole fractions are from Sack & Ghiorso (1991a, 1991b) and reported in Table. A1. The molar Gibbs energy $\overline{G}$ is calculated from the vibrational Gibbs energy $\overline{G}^*$ and the ideal molar configurational entropy $\overline{S}^{IC}$ as:

$$\overline{G} = \overline{G}^* - T\overline{S}^{IC} \tag{A.7}$$

A second-degree Taylor expansion of the compositional and ordering variables is used to describe the molar vibrational Gibbs energy as (Thompson Jr., 1969):

$$\overline{G}^* = g_0 + \sum_i \left(g_i X_i + g_{ii} X_i^2 + \sum_{j<i} g_{ij} X_i X_j \right)$$
$$+ \sum_i \sum_k \left(g_{ik} X_i s_k \right)$$
$$+ \sum_k \left(g_k s_k + g_{kk} s_k^2 + \sum_{l<k} g_{kl} s_k s_l \right) \tag{A.8}$$

where *g* terms are Taylor coefficients from Table 3 in Sack & Ghiorso (1991b). The configurational entropy is calculated from compositional variables and site fractions as:

$$\overline{S}^{IC} = -R \sum_r \sum_c \overline{r} X_{c,r} \ln X_{c,r} \tag{A.9}$$

where $X_{c,r}$ is the fraction of cation *c* in site *r* in terms of X_i and s_i, and $\overline{r}$ is the number of *r* sites per formula unit. A Darken equation is then used to manipulate and express the chemical potential of the spinel endmembers (Darken & Gurry, 1953; Sack, 1982; Ghiorso, 1990; Sack & Ghiorso, 1991a):

$$\mu_j = \overline{G} + \sum_i n_{i,j} (1 - X_i) \left(\frac{\partial \overline{G}}{\partial X_i} \right)_{\frac{X_k}{X_i}, s_m} + \sum_i (q_{ij} - s_i) \left(\frac{\partial \overline{G}}{\partial s_i} \right)_{X_k, s_l} \tag{A.10}$$

where $n_{i,j}$ and $q_{i,j}$ represent coefficients of X_i and s_i, respectively, in 1 mol of spinel component *j*. The chemical potential of component $MgAl_2O_4$ in a spinel solution can be written as:

$$\mu_{MgAl_2O_4}^{Spl} = \overline{G}_2^* + RT\ln \left[(X_2) / (1 + X_4) (1 - X_3 - X_4 - X_5)^2 \right]$$
$$+ W_{Fe-Mg}^{TET} (1 - X_2)(1 + X_4 - X_2)$$
$$+ \Delta\overline{G}_{23}^0 (1 - X_2)(X_3) + \Delta\overline{G}_{24}^0 (1 - X_2)(X_4) + \Delta\overline{G}_{25}^0 (1 - X_2)(X_5)$$
$$+ W_{1'3'} X_3 (X_3 + X_4 + X_5)$$
$$+ W_{1'4'} X_4 (X_3 + X_4 + X_5)$$
$$+ W_{1'5'} X_5 (X_3 + X_4 + X_5)$$
$$- W_{3'4'} (X_3)(X_4) - W_{3'5'} (X_3)(X_5)$$
$$- W_{4'5'} (X_4)(X_5) \tag{A.11}$$

where $\overline{G}_2^*$ is the vibrational Gibbs energy of the $MgAl_2O_4$ endmember. The Gibbs energy along joins between vertices differing in composition (i.e. $\Delta\overline{G}_{23}^0$, $\Delta\overline{G}_{24}^0$, and $\Delta\overline{G}_{25}^0$) are standard state Gibbs free energies of the Mg-Fe exchange reactions between aluminate (G_2), chromate (G_3), titanate (G_4), and ferrite spinel (G_5). W_{Fe-Mg}^{TET}, W_{ij}, and $W_{ij'}$ are symmetric regular solution parameters describing deviations of the Gibbs energy from ideal mixing. To focus on Al partitioning between olivine and spinel, we combine Eqs. A.2, A.6, and A.10 with independent parameters X_i (Table A1) as:

$$\mu_{MgAl_2O_4^{Ol}}^0 + RT\ln \left[\gamma \times \left(Al_2O_{3\ wt.\%}^{Ol} / M_{Al_2O_3} \right) \times M_{MgAl_2O_4} \right]$$
$$= \overline{G}_2^* + RT\ln \left[(X_2) / (1 + X_4)(1 - X_3 - X_4 - X_5)^2 \right]$$
$$+ W_{Fe-Mg}^{TET} (1 - X_2)(1 + X_4 - X_2)$$
$$+ \Delta\overline{G}_{23}^0 (1 - X_2)(X_3) + \Delta\overline{G}_{24}^0 (1 - X_2)(X_4) + \Delta\overline{G}_{25}^0 (1 - X_2)(X_5)$$
$$+ W_{1'3'} X_3 (X_3 + X_4 + X_5)$$
$$+ W_{1'4'} X_4 (X_3 + X_4 + X_5)$$
$$+ W_{1'5'} X_5 (X_3 + X_4 + X_5)$$
$$- W_{3'4'} (X_3)(X_4) - W_{3'5'} (X_3)(X_5)$$
$$- W_{4'5'} (X_4)(X_5) \tag{A.12}$$

Table A2: Coefficients and statistical parameters of regressions for OSAT

	Coefficients[a]	Statistical parameters	
		Eq. 5	
c0	−0.168	r^2	0.97
c1	1.487	SEE	20.20
c2	−0.593	RMSE	29.00
c3	−0.630	P value	1.11E-16
c4	0.390	r^2_{MCCV}	0.97
c5	0.009	SEE_{MCCV}	20.20
c6	−2.492	$RMSE_{MCCV}$	23.90
c7	0.065		
c8	−0.031		
c9	−4.141		
c10	−0.428		
c11	−4.637		
c12	−0.054		
c13	−10.803		
c14	2.714		
b	0.654		
		Eq. 7	
Cr#	1.144 (0.136)	r^2	0.83
$\ln K_{D_{Al}}$	−0.865 (0.046)	SEE	44.80
const	0.740 (0.317)	RMSE	34.40
		P value	2.88E-36
		r^2_{MCCV}	42.10
		SEE_{MCCV}	0.92
		$RMSE_{MCCV}$	43.30
		Eq. 8	
Cr#	0.543 (0.121)	r^2	0.91
$\ln K_{D_{Al}}$	−0.657 (0.040)	SEE	31.70
$\ln K_{D_{Cr}}$	−0.389 (0.041)	RMSE	39.10
const	0.049 (0.241)	P value	3.79E-47
		r^2_{MCCV}	0.94
		SEE_{MCCV}	35.80
		$RMSE_{MCCV}$	34.20

[a]number in bracket indicates the 1σ error of coefficients for the linear regression.

After re-organizing terms:

$$RT\ln\left[\gamma \times Al_2O_3^{Ol}{}_{wt\%}/\left((X_2)/(1+X_4)(1-X_3-X_4-X_5)^2\right)\right]$$

$$= \overline{G}_2^* - \mu^0_{MgAl_2O_4^{Ol}}$$

$$+W_{TET}(1-X_2)(1+X_4-X_2)$$

$$+\Delta\overline{G}^0_{23}(1-X_2)(X_3)+\Delta\overline{G}^0_{24}(1-X_2)(X_4)+\Delta\overline{G}^0_{25}(1-X_2)(X_5)$$

$$+W_{1'3'}X_3(X_3+X_4+X_5)$$

$$+W_{1'4'}X_4(X_3+X_4+X_5)$$

$$+W_{1'5'}X_5(X_3+X_4+X_5)$$

$$-W_{3'4'}(X_3)(X_4)-W_{3'5'}(X_3)(X_5)$$

$$-W_{4'5'}(X_4)(X_5) \qquad (A.13)$$

On the left side of Eq. A.13, $(X_2)/(1+X_4)(1-X_3-X_4-X_5)^2$ is equal to $X^{TET}_{Mg^{2+}}X^{OCT}_{Al^{3+}}{}^2$; on the right side of Eq. A.13, all parameters are constants or barely change with temperature (see Sack & Ghiorso, 1991a), except $\mu^0_{MgAl_2O_4^{Ol}}$, $\overline{G}_2^*$ and the independent composition X_i. $\overline{G}_2^*$ can be rewritten as $\left(c_1X_2+c_2X_2^2+c_3X_2^{\frac{1}{2}}\right)$ following Eq. A.8, where c_1, c_2 and c_3 are constants derived from the Taylor

expansion coefficients. However, given that the standard state of $MgAl_2O_4$ (i.e. $\mu^0_{MgAl_2O_4^{Ol}}$) in olivine is not well constrained, $\mu^0_{MgAl_2O_4^{Ol}}$, by definition, is relevant to temperature at any given pressure and composition. We thus simplified $\mu^0_{MgAl_2O_4^{Ol}}$ to be a function of temperature and independent of olivine composition given the trace concentration of Al in olivine (Ganguly, 2008), and γ for Al_2O_3 in olivine can be assumed to be 1. We thus encapsulate all parameters related to spinel as φ^{Spl}, and Eq. A.13 can be fitted with coefficients (c_i) replacing the regular solution parameters, and related to the spinel composition as:

$$\ln\left(\frac{X_{Al_2O_3^{Ol}}}{X^{TET}_{Mg^{2+}}X^{OCT}_{Al^{3+}}}\right)+b=\frac{\varphi^{Spl}}{c_0 \times T} \qquad (A.14)$$

where

$$\varphi^{Spl}=c_1X_2+c_2X_2^2+c_3X_2^{\frac{1}{2}}$$

$$+c_4(1-X_2)(1+X_4-X_2)$$

$$+c_5(1-X_2)(X_3)+c_6(1-X_2)(X_4)+c_7(1-X_2)(X_5)$$

$$+c_8X_3(X_3+X_4+X_5)$$

$$+c_9X_4(X_3+X_4+X_5)$$

$$+c_{10}X_5(X_3+X_4+X_5)$$

$$-c_{11}(X_3)(X_4)-c_{12}(X_3)(X_5)-c_{13}(X_4)(X_5)+c_{14}$$

The coefficients b, and $c_0–c_{12}$ can be then obtained by fitting the compositions of experimental olivine and spinel pairs.

APPENDIX B. F-TEST MODEL

An *F*-test is a statistical test with the null hypothesis that a distribution follows an *F* distribution; The *F*-test has been used in solving geological problems involving regression (e.g. Abouchami *et al., 2005*). An *F*-test is commonly used to compare two models that give similar or identical results but use different numbers of parameters, with the aim of determining which model is statistically better or whether the model with fewer parameters is nested within the model with more parameters. In this case, the *F* value can be calculated as:

$$F = \frac{(RSS_1 - RSS_2) / (p_1 - p_2)}{RSS_2 / (n - p_2)} \tag{B.1}$$

where RSS_i represents the residual sum of squares of model i; p_1 and p_2 represent the number of parameters in models 1 (m_1) and 2 (m_2), and $p_1 < p_2$; and n is the amount of data points used in the regressions. While comparing the two models, the null hypothesis is that m_2 is not better than m_1 (i.e. that m_2 is an overfitting of m_1). When comparing the *F* value with the critical *F* value, which can be calculated from the *F* distribution with $(p_2 - p_1, n - p_2)$ degrees of freedom, if *F* exceeds the critical value, the associated *P* value is small ($<1 - A$; e.g. A = 0.05 for 95% confidence) and then null hypothesis is rejected, meaning that m_2 is indeed statistically better. If *F* is below the critical value, the associated *P* value is larger than A and m_1 is statistically better than m_2.